molecules

MDPI

Article

Microporous Activated Carbon from *Pisum sativum* Pods Using Various Activation Methods and Tested for Adsorption of Acid Orange 7 Dye from Water

Mohamed A. El-Nemr [1], Ahmed El Nemr [2,*], Mohamed A. Hassaan [2], Safaa Ragab [2], Luigi Tedone [3], Giuseppe De Mastro [3] and Antonio Pantaleo [3]

[1] Department of Chemical Engineering, Faculty of Engineering, Minia University, Minia 61519, Egypt; mohamedelnemr1992@yahoo.com
[2] National Institute of Oceanography and Fisheries (NIOF), Marine Pollution Lab, Alexandria 21556, Egypt; mhss95@mail.com (M.A.H.); safaa_ragab65@yahoo.com (S.R.)
[3] Department of Agriculture and Environmental Sciences, Bari University, 70121 Bari, Italy; luigi.tedone@uniba.it (L.T.); giuseppe.demastro@uniba.it (G.D.M.); antonio.pantaleo@uniba.it (A.P.)
* Correspondence: ahmedmoustafaelnemr@yahoo.com or ahmed.m.elnemr@gmail.com

Highlights:

- *Pisum sativum* pods was used for producing porous activated carbon materials.
- Two chemical methods and two gases were used in the activation processes.
- Higher performances were achieved by applying $ZnCl_2$ and CO_2 for activation.
- The products exhibited large surface areas and high AO7 dye adsorption performances.
- RMS study of the AO7 dye removal by produced material was reported.

Abstract: This work demonstrates the preparation of high-surface-area activated carbon (AC) from *Pisum sativum* pods using $ZnCl_2$ and KOH as activating agents. The influence of CO_2 and N_2 gases during the carbonization process on the porosity of AC were studied. The highest specific surface area of AC was estimated at 1300 to 1500 m^2/g, which presented characteristics of microporous materials. SEM micrographs revealed that chemical activation using an impregnation reagent $ZnCl_2$ increases the porosity of the AC, which in turn leads to an increase in the surface area, and the SEM image showed that particle size diameter ranged between 48.88 and 69.95 nm. The performance of prepared AC for adsorption of Acid Orange 7 (AO7) dye was tested. The results showed that the adsorption percentage by AC (2.5 g/L) was equal to 94.76% after just 15 min, and the percentage of removal increased to be ~100% after 60 min. The maximum adsorption capacity was 473.93 mg g^{-1}. A Langmuir model (LM) shows the best-fitted equilibrium isotherm, and the kinetic data fitted better to the pseudo-second-order and Film diffusion models. The removal of AO7 dye using AC from *Pisum sativum* pods was optimized using a response factor model (RSM), and the results were reported.

Keywords: microporous; activated carbon; pea pods; *Pisum sativum*; Acid Orange 7 dye; pyrolysis; removal

check for updates

Citation: El-Nemr, M.A.; El Nemr, A.; Hassaan, M.A.; Ragab, S.; Tedone, L.; De Mastro, G.; Pantaleo, A. Microporous Activated Carbon from *Pisum sativum* Pods Using Various Activation Methods and Tested for Adsorption of Acid Orange 7 Dye from Water. *Molecules* **2022**, *27*, 4840. https://doi.org/10.3390/molecules27154840

Academic Editors: Giuseppe Cirillo and Hom Nath Dhakal

Received: 30 June 2022
Accepted: 21 July 2022
Published: 28 July 2022

Publisher's Note: MDPI stays neutral with regard to jurisdictional claims in published maps and institutional affiliations.

1. Introduction

Rapid urbanization and the expansion of factories in varied locations pose a huge challenge to humankind in this century in the form of water pollution issues. As a result, treating aquatic pollutants is frequently a difficult task. This is due to the large number of structurally diverse pollutants that can interact with a variety of natural and anthropogenic sources, dissolved or particulate chemical species, light, and even living organisms, causing significant ecosystem disruption [1–3]. As a result of rapid urbanization and the proliferation of factories in various environments, water pollution is one of the most dangerous threats we face in this era [4]. Because water pollution has an impact on all living species and populations as well as on the overall performance of the aquatic

ecosystem, the fact that dyes are difficult to remove from the water system, stable, and non-biodegradable makes them dangerous water pollutants for the most part [5,6]. The dying, textile, leather, printing, cosmetics, food processing, and paper-making sectors all produce dye-contaminated wastewater. The harmful and carcinogenic consequences of these colored effluents' discharge onto living organisms make them a serious environmental issue [7,8]. Globally, roughly 7×10^5 tons of dyes (seven distinct types of dyes) are produced each year, and about 10–15% of the dye used in the process is lost in the discharged effluent [9,10]. Due to the hazardous and carcinogenic nature of these effluents, they should never be released into the environment. It is possible to classify dyes into anionic (acid, direct, and reactive dyes) and non-ionic (vat dyes and disperse dyes) categories based on their solubility in water [11–13]. Basic dyes can be used to color acrylic fibers, acid dyes to color wool, silk, or nylon, and disperse dyes to color polyester or nylon with. Cotton fibers should only be dyed using vat or reactive dyes. Dye hydrolysis creates intensely colored wastewater effluents that are contaminated. When using vat dyes, it is necessary to reduce them in an alkaline medium with potent reduction agents, such as sodium hydrosulfite, before they can cling to the textile substrate [14]. The majority of dyeing methods employ a variety of pollutant-generating additives. Water dyes not only reduce sunlight penetration and thus photosynthesis, but they may also impede aquatic biota growth and reduce the solubility of gases in water [15,16]. Conventional wastewater treatment systems have difficulty removing many colors from water because they are nonbiodegradable and persistent under light, heat, and some oxidizing agents [17]. Efficient dye removal from aqueous solution by high-performance electrospun nanofibrous membranes through incorporation of SiO_2 nanoparticles has been reported [18]. Activated carbon is a porous structure material showing amphoteric characteristics. Therefore, it is used for adsorption of inorganic and organic compounds such as dyes. There are some notable advantages of activated carbon (AC), such as low production cost, high surface reactivity, significant thermal stability, active free valances, and the applicability of its high capacity and high rate of adsorption [19]. Both powdered (approximately 44 µm) and granulated (particle size 0.6–4.0 mm) forms of activated carbon can be obtained [20,21]. Activated carbon can be divided depending on its pore size into microporous (<2 nm), mesoporous (2–50 nm), and macroporous (>50 nm) groups, which can be controlled during the preparation process of activated carbon for specific applications [22,23]. There are two primary methods for activating carbon compounds: physical and chemical. Chemical activation uses higher temperatures, which make physical activation more efficient. As a result, improvements in activated carbon's porous structure have been made when using a chemical activation approach [20,24]. The physical activation process is performed in two steps. The first step is carbonization to produce non-porous char. The second step is the activation with carbon dioxide (CO_2), N_2, or the flow of steam [25]. Chemical activation can be performed in one step by applying raw material thermal decomposition with chemical reagents. Chemical reagents used in the activation processes are either acidic reagents, such as zinc chloride ($ZnCl_2$) [13,14], phosphoric acid (H_3PO_4) [26], hydrochloric acid (HCl) [27], and sulfuric acid (H_2SO_4) [28] or basic reagents such as potassium hydroxide (KOH) [29], potassium carbonate (K_2CO_3) [30], sodium hydroxide (NaOH) [31], and sodium carbonate (Na_2CO_3) [32]. Acid-based activation processes lead to the formation of -COO groups on the surface of activated carbon in addition to increasing its surface area [32]. The negatively charged carboxylic groups increase the ability of carbon to adsorb heavy metals, such as lead, cadmium, cobalt, and mercury. Additionally, acid activation leads to a decrease in ash content in activated carbon and enhanced activated carbon properties [33].

Activated carbon's price continues to rise due to the increased use of this material in a variety of processes, including adsorption, fuel cells, gas storage, and catalysis, to name a few. Therefore, the search for new, easily available, and cheap resources for the production of activated carbon is an important goal. Due to their availability, renewable nature, and ability to reduce environmental pollution, agricultural leftovers have received considerable interest as raw materials for synthesizing activated carbon [34]. Therefore,

many agricultural-plant-based materials, such as cotton hull, sago industry waste, banana pith [35], sawdust [36–38], fiber [39], shells from different sources [40–42], palm [43], date pit [44], rice bran [45], coir pith [46], mango seed [47], straw [48], coconut coir dust [49], pine cone [50], wheat husk [51], pomegranate husk [28], banana trunk waste [52], and spent coffee grounds [53] have been used for the production of AC for wastewater treatment. Due to the multiple uses of AC, many researchers attempted different methods to reduce the cost of activated carbon production by generating carbon from cheap available sources or by performing surface modification. However, few research works have been reported for the use of pea skin for production of activated carbon [54].

The use of *Pisum sativum* pea pods for the preparation of microporous activated carbon using different chemical activations under flow of N_2 and CO_2 was investigated. The prepared activated carbon with the highest surface area was used to study the uptake of Acid Orange 7 (AO7) dye from artificial wastewater. AO7 dye removal was investigated as a function of several variables, including temperature, initial dye concentration, adsorbent concentration, and contact time. Different isotherm and kinetic models were used to calculate and explain the adsorption isotherms and kinetic parameters, which were then explored in detail.

2. Results and Discussion

2.1. Effect of Impregnation Reagent, Activation Temperature, and Activating Reagent

For the preparation of activated carbon, different processes were performed by chemical activation with a 2:1 ratio of $ZnCl_2$ and with 10% KOH. Additionally, the carbonaceous precursor was activated by carbon dioxide and nitrogen gases under different temperatures (600, 700, and 800 °C) for 1 h. These impregnation reagents and their ratio have been chosen according to our previous study. According to the experimental results, the type of impregnation reagent is the critical parameter among the operational parameters of the activation reaction in order to prepare *Pisum sativum* pods as activated carbon (AC), as it has a significant effect on the specific surface area, monolayer volume, mean pore diameter, total pore volume, and adsorption capacity of the activated carbon.

We investigated the effect of activation temperature on the AC yield. The yield of activated carbon reduced from 36.11 to 20.94% and from 37.61 to 18.89%, respectively, when 10% KOH was activated with N_2 and CO_2 gases at activation temperatures of 600 to 800 °C. From the previous results, we deduced that the yield of activated carbon decreased because the KOH may have accelerated the evaporation of volatile compounds through the breakdown of aromatic and aliphatic chains. However, a slight decrease in yield from 43.61 to 31.58% was observed by using a 2:1 ratio of $ZnCl_2$ under CO_2 gas at activation temperatures (600–800 °C). On the other hand, under N_2 gas, differences in the activated carbon yield at the activation temperatures 600 to 800 °C were not observed. Generally, the yield of AC-KOH is smaller than other AC-$ZnCl_2$ samples. The reason for this could be that the zinc chloride acts as a dehydrating agent which enhanced the removal of volatiles such as H_2 and O_2 from the carbon matrix.

Chemical activation was used to evaluate the effects of KOH and $ZnCl_2$ on the carbonization of activated carbon from *Pisum sativum* pods. Table 1 summarizes the preliminary findings. The results indicated that utilizing impregnation agents $ZnCl_2$ and 10% KOH for chemical activation, as well as activating agents N_2 and CO_2 gases at activation temperatures of 600, 700, and 800 °C, can result in considerable changes in the surface area and pore volume of the final activated carbon. These results may be due to the difference in roles and activation mechanisms for both of them as chemical reagents during the carbonization process. The activation by KOH under CO_2 flow slightly improved the porous structure (specific surface area and pore volume), while for activation under N_2, the pore volume and specific surface area were much improved. Scheme 1 shows the KOH activation mechanism [55]. According to the KOH activation mechanism and earlier findings, we concluded that because KOH is a strong base, it can interact directly with carbon atoms and so catalyze dehydrogenation and oxidation processes, resulting in carbon consumption, tar suppression, and the formation of pores [56].

Table 1. Surface area analysis using different models of activated carbons prepared under different conditions.

Analysis Method		BET						t-Plot		MP		BJH ads		BJH des	
Sample Entry	Carb. Temp.	AC Yield	$a_{s,\ BET}$ (m^2/g)	V_m (cm^3/g)	Mean Pore Diameter	Total Pore Volume	a_1-a_2 (m^2/g)	V2	2t (nm)	a_1-a_2 (m^2/g)	V_p (cm^3/g)	V_p	a_p	V_p	a_p
		(%)	S_{BET} (m^2/g)	V_m (cm^3/g)	D_p (nm)	V_T (cm^3/g)	S_{mi} (m^2/g)	V_{mi} (cm^3/g)	2t (nm)	(m^2/g)	(cm^3/g)	(cm^3/g)	(m^2/g)	V_{me} (cm^3/g)	S_{me} (m^2/g)
KOH/CO_2	600	37.61	357.82	82.21	2.068	0.185	420.11	0.156	0.740	392.47	0.163	0.055	45.16	0.028	45.16
	700	23.44	87.70	20.15	2.974	0.065	82.33	0.039	0.933	81.30	0.040	0.038	27.32	0.019	27.32
	800	18.89	241.84	55.57	2.462	0.149	254.40	0.119	0.929	244.50	0.119	0.070	67.34	0.020	67.34
KOH/N_2	600	36.11	197.33	45.34	2.332	0.115	205.43	0.086	0.827	212.23	0.091	0.046	35.25	0.019	5.31
	700	24.17	716.28	164.57	1.938	0.347	879.53	0.248	0.560	804.12	0.302	0.081	48.13	0.072	31.75
	800	20.94	914.58	210.13	1.772	0.405	1146.78	0.373	0.647	1029.38	0.392	0.065	56.66	0.038	21.78
$ZnCl_2/CO_2$	600	43.61	1228.00	282.13	1.799	0.552	1480.09	0.532	0.714	1373.09	0.544	0.089	94.87	0.053	40.38
	700	41.35	1092.70	251.06	1.859	0.508	1281.39	0.487	0.756	1208.81	0.498	0.097	110.18	0.052	39.60
	800	31.58	1299.40	298.55	1.901	0.618	1479.36	0.595	0.799	1426.09	0.611	0.127	152.44	0.058	44.15
$ZnCl_2/N_2$	600	39.85	1039.50	238.83	1.915	0.498	1214.95	0.455	0.745	1143.14	0.466	0.110	110.16	0.069	50.17
	700	39.84	1064.00	244.47	1.805	0.480	1286.20	0.457	0.706	1188.57	0.469	0.078	79.96	0.050	36.06
	800	39.85	1084.20	249.11	1.767	0.479	1316.97	0.460	0.694	1217.64	0.476	0.068	69.96	0.043	31.16

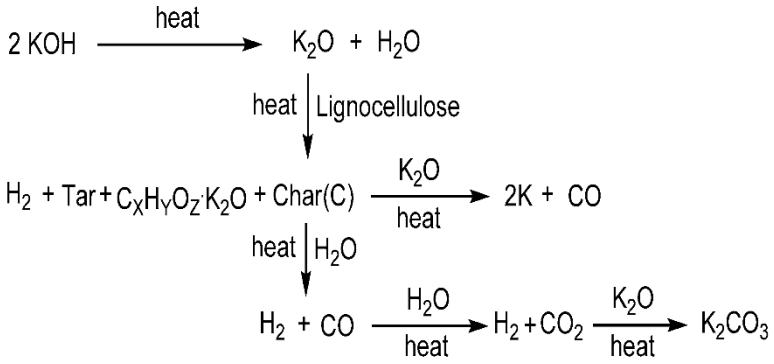

Scheme 1. The KOH activation mechanism.

However, the random distribution of KOH inside the matrix of *Pisum sativum* pods may result in hyperactivation after heat treatment, collapsing the pore walls and resulting in the enlargement of micropores into mesopores. Additionally, the results in Table 1 show that $ZnCl_2$ as an impregnation reagent under CO_2 and N_2 gases is more effective in pore development and in increasing specific surface area than KOH. Scheme 2 illustrated the $ZnCl_2$ activation mechanism. $ZnCl_2$ is considered a Lewis acid, so it has a completely different activation mechanism from the KOH activation mechanism. $ZnCl_2$ can act as a strong dehydrating agent, which can easily interact with the oxygen atom in OH functional groups in lignocelluloses substances (*Pisum sativum* pods), causing a dehydration reaction and dehydrogenation from the hydroaromatic structure. Furthermore, during the heat treatment, $ZnCl_2$ fused and reacted with H_2O, forming the zinc oxide chloride hydrate ($Zn_2OCl_2{\cdot}2H_2O$). Most importantly, due to increasing the temperature, the $Zn_2OCl_2{\cdot}2H_2O$ decomposed and the $ZnCl_2$ gas could evolve, which played an important role in the formation of many new sites, subsequent growth in the pore structure, and creation of the porosity in the final product. Additionally, $ZnCl_2$ gas hinders the formation of tar inside the formed pores [57,58].

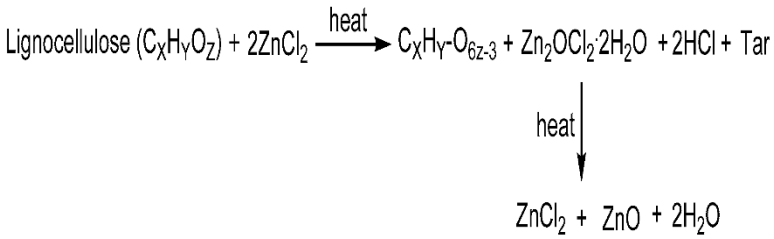

Scheme 2. The $ZnCl_2$ activation mechanism.

2.2. Characterization of Activated Carbon

2.2.1. The X-ray Diffraction

Figure 1a shows the XRD patterns of raw pea pods impregnated with KOH (RPP-KOH) and activated carbon prepared by pyrolysis at 800 °C under flow of CO_2 (AC-KOH). The XRD pattern for the sample RPP-KOH displays two small broad diffraction peaks around 24° and 44°, corresponding to the (002) and (100) diffractions for carbon. The XRD pattern for sample AC-KCO showed a broad diffraction peak located at 2θ = 24°, and another peak at 2θ = 44°, which became markedly sharper. According to this peak, it is possible that the activated carbons contain potassium compounds with high crystallinity after being activated with KOH. K metal was created mostly during the activation process at temperatures above 700 °C [59]. The XRD patterns of raw pea pods impregnated with $ZnCl_2$ (RPP-$ZnCl_2$) and its activated carbon prepared by pyrolysis at 800 °C under flow of CO_2 (AC-$ZnCl_2$-CO_2) are shown in Figure 1b. The RPP-$ZnCl_2$ sample showed a broad diffraction peak located at 2θ = 22° and a small intensity peak at 44°. The AC-$ZnCl_2$-CO_2 sample's XRD pattern revealed a minor shift in the peak from 22° to 25°, indicating the

presence of an amorphous structure with unevenly stacked carbon rings that are helpful for forming an adsorption gap. Additionally, the peak at 44° became somewhat sharp, indicating that AC-$ZnCl_2$-CO_2 had a more orderly structure than RPP-$ZnCl_2$ and that the activation process may possibly promote the formation of graphite microcrystallites. Ultimately, the peaks between 10° and 20° are attributed to the presence of micropores and microcrystallinity in the synthesized activated carbon [60], which could be related to the graphite-like microcrystalline structure of multilayer stacks [55].

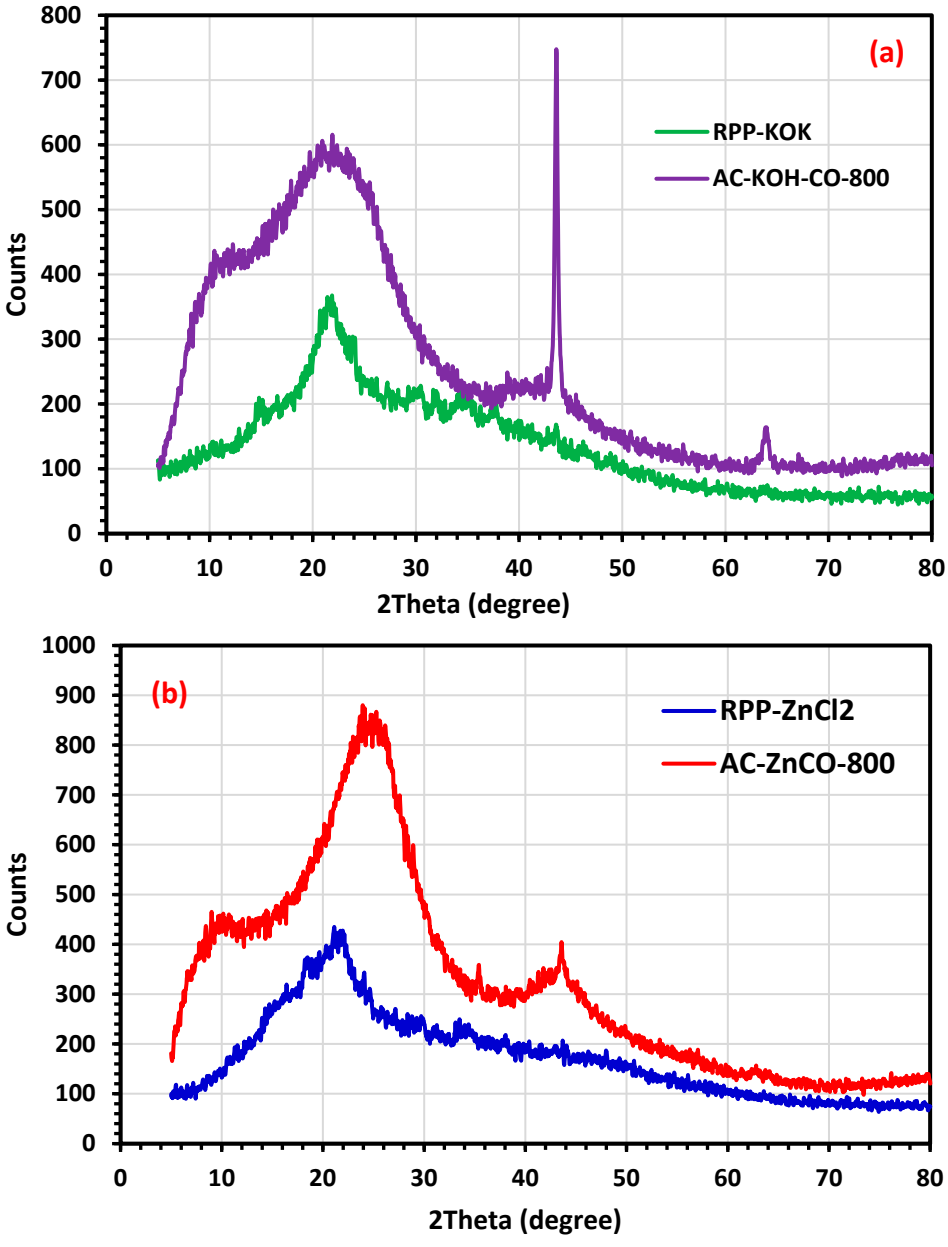

Figure 1. XRD analysis of (**a**) raw pea pods (*Pisum sativum*) impregnated with KOH (green) and activated carbon prepared with it via pyrolysis at 800 °C under flow of CO_2 (purple); (**b**) raw pea pods (*Pisum sativum*) impregnated with $ZnCl_2$ (blue) and activated carbon prepared with it via pyrolysis at 800 °C under flow of CO_2 (red).

2.2.2. FTIR- Spectra

Figures 2a–d and 3a–c showed the FTIR spectra of raw pea pods (*Pisum sativum*) (RPP), the raw pea pods impregnated with a 2:1 ratio of $ZnCl_2$ (RPP-$ZnCl_2$) and with 10% KOH (RPP-KOH) samples, and activated carbon prepared by pyrolysis at 800 °C under flow of

N_2 and CO_2 (AC-ZnN and AC-ZnCO), respectively. We observed that all the spectra in Figures 2a–d and 3a–c are similar. The development of a broad band around 3290 cm^{-1} correlates to hydroxyl (OH)-stretching vibration functional groups, which vanished when the temperature was increased to 800 °C. At 2850 cm^{-1}, the presence of a faint band suggests the presence of an aliphatic −CH-stretching vibration, which was totally abolished at 800 °C. The emergence of a very weak peak at about 2650 cm^{-1} following activation at 800 °C was demonstrated to correspond to the existence of stretching (C-H aldehydes). The appearance of a minor peak around 2300–2350 cm^{-1} that is linked to C≡C-stretching vibrations in alkyne groups (Figures 2c and 3b). In the case of activated carbon formed by pyrolysis at 800 °C with a 2:1 ratio of $ZnCl_2$ under CO_2 flow, the steep peak at 1600 cm^{-1} correlates to C=C skeletal stretching of the aromatic rings, which was more pronounced than when the activated carbon was generated under N_2 flow. Due to the decomposition of C−H bonds at the higher activation temperature (800 °C) to generate more stable aromatic C=C bonds, this peak may become sharper with $ZnCl_2$ under CO_2 flow. C=O, C–O of carboxylic groups, or in-plane vibration of O−H of carboxylic groups can all be blamed for the appearance of a peak at 1400 cm^{-1}. During the aromatization of pea pods at 800 °C as the activation temperature, this peak was completely erased. The stretching vibration of the C–O group in carboxylic acids, alcohols, phenols, ethers, esters, or the P=O bond in phosphate esters matched to the broad peaks at around 1050–1200 cm^{-1}. C−C stretching may be responsible for the peaks around 700–400 cm^{-1}. The small absorption peak at 600 cm^{-1} could be attributed to Si-H-stretching vibrations or benzene polycyclic and C−H bending, which are also possible explanations. Following the activation procedure, the majority of the functional group's adsorption peak was eliminated, and new peaks emerged. This could be due to the feedstock's functional groups evaporating as volatile molecules when heated, indicating that the activation process has been completed properly [61].

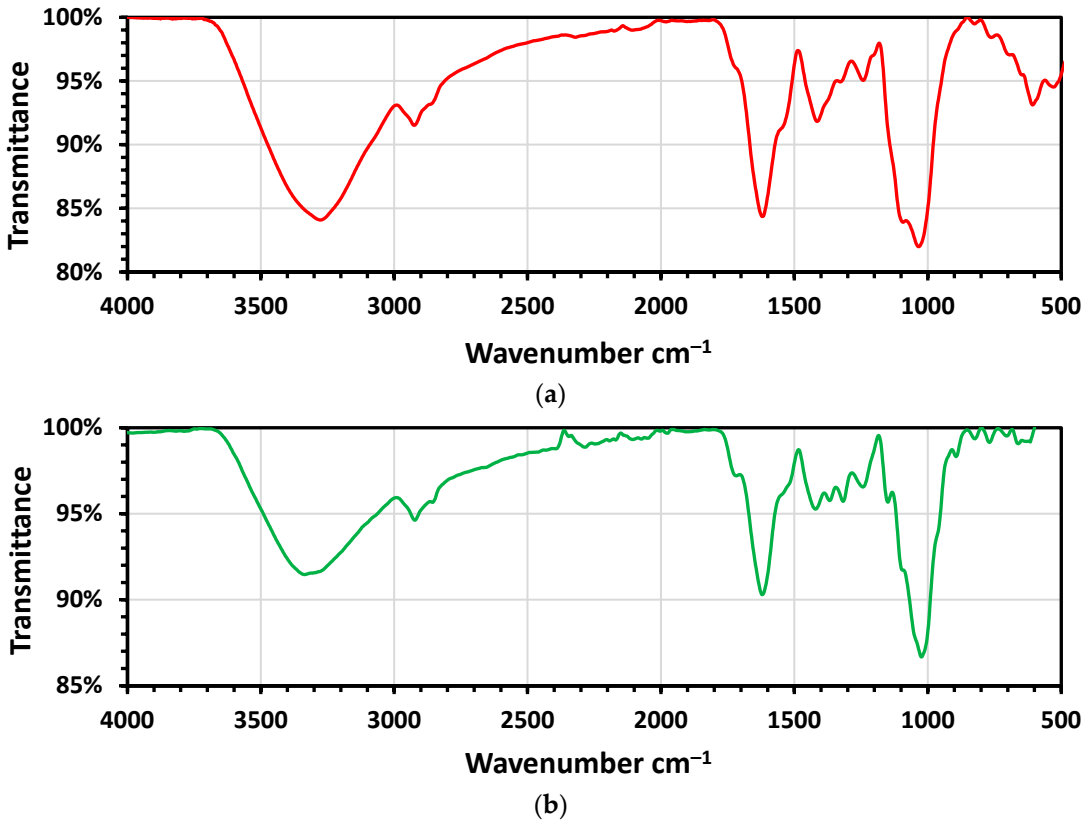

Figure 2. *Cont.*

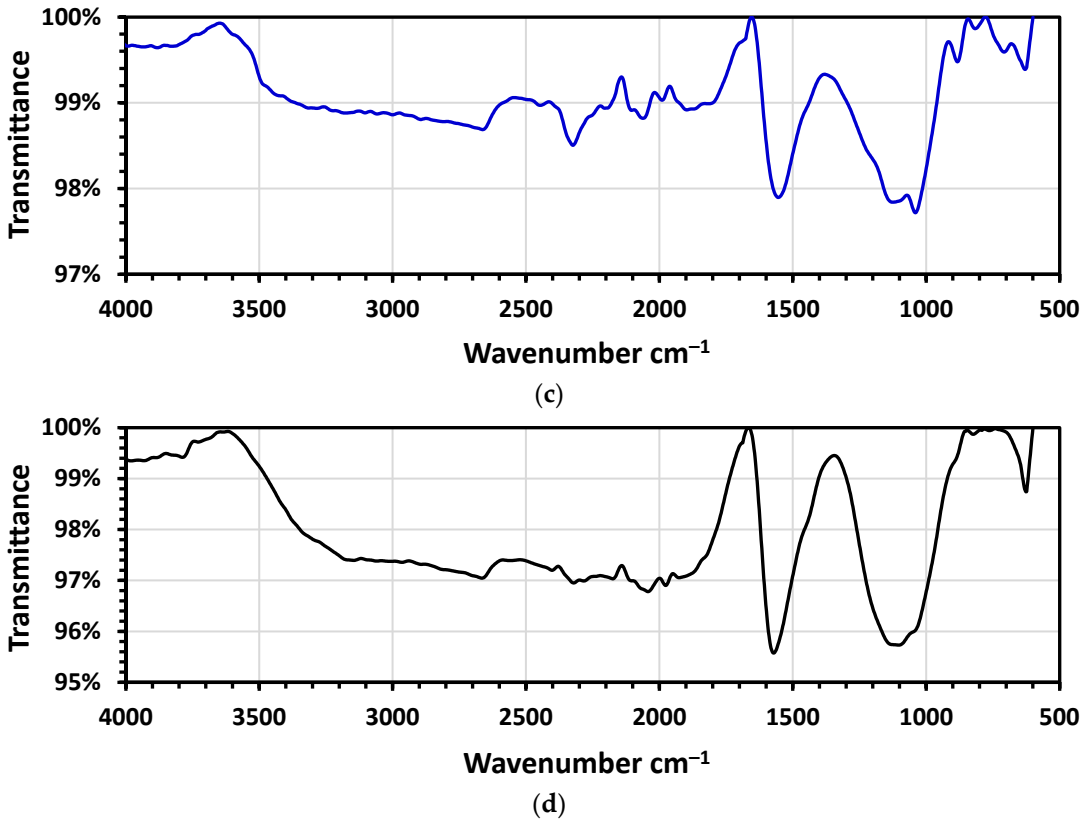

Figure 2. FTIR analysis of (**a**) raw pea pods, (**b**) raw pea pods–$ZnCl_2$, (**c**) AC-$ZnCl_2$/N_2/800, (**d**) AC-$ZnCl_2$/CO_2/800 °C.

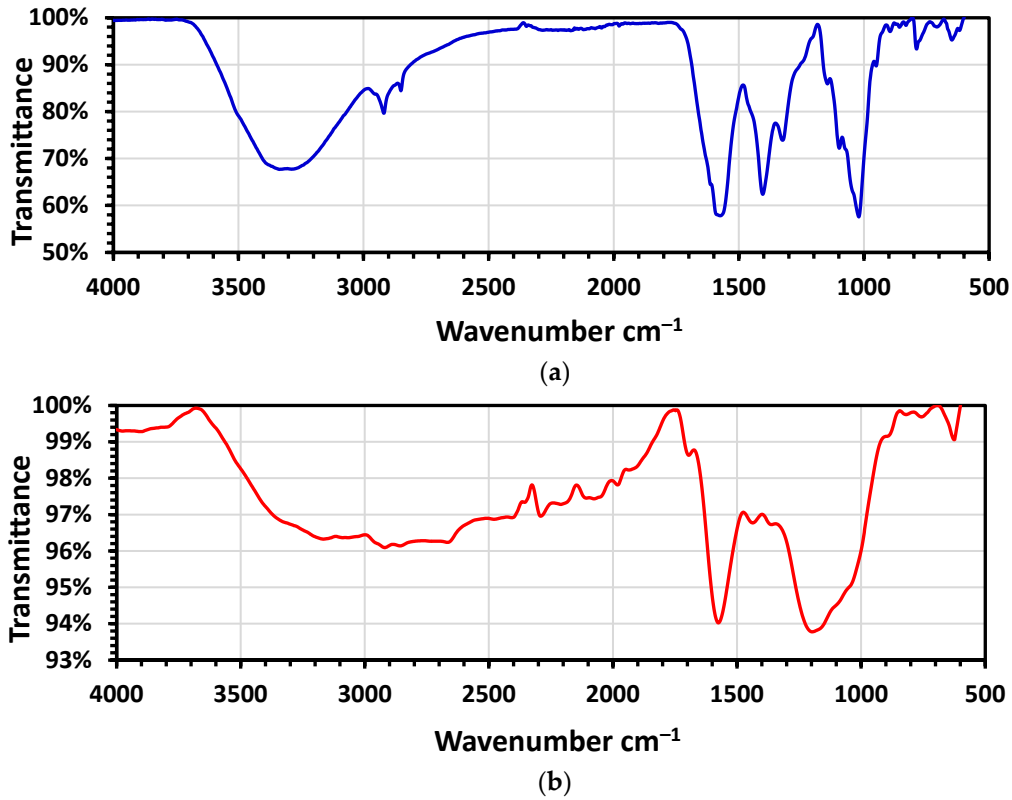

Figure 3. *Cont.*

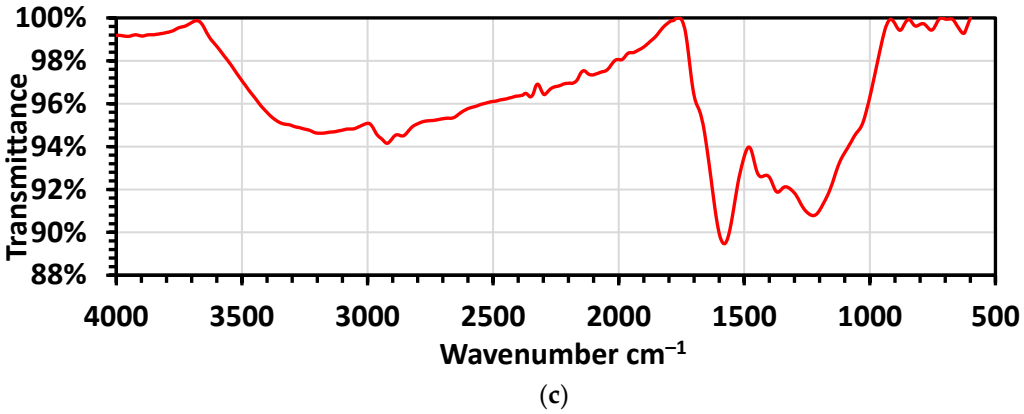

(**c**)

Figure 3. FTIR analysis of (**a**) raw Pea pods–KOH, (**b**) AC-KOH/N_2/800 °C, (**c**) AC-KOH/CO_2/800 °C.

2.2.3. Scanning Electron Microscopy (SEM)

Figure 4a–f shows the SEM images of the microstructure of the *Pisum sativum* pods, which were impregnated with a 2:1 ratio of $ZnCl_2$ and activated at different temperatures (600, 700, and 800 °C) under CO_2 gas for 60 min. It can be seen from SEM images taken during the activation stage (700 °C) that several porous and hollow carbon holes were observed on the activated carbon's surface. The external surface of the activated carbon has a porous structure with a large number of micropores because the most volatile organic materials evolved. Micrographs (~nm range) of activated carbon taken during experiments performed at carbonization temperatures 600 and 800 °C exhibit an extensive external surface with a very high number of micropores with diameters ranging from 69.95–48.88 nm, which act as channels for the microporous adsorbent. Obviously, activated carbon processes were successful, and the microporous structure was developed by chemical activation process with $ZnCl_2$, so it had a large specific surface area, which was consistent with the BET value.

2.2.4. The Thermogravimetric Analysis (TGA and DTA)

The TGA and DTA profiles of the raw pea pods (*Pisum sativum*) (RPP) and their impregnation with a 2:1 ratio of $ZnCl_2$ (RPP-$ZnCl_2$) and with 10% KOH (RPP-KOH) samples give an excellent vision about the range of carbonization temperatures needed to produce the activated carbon. The TGA and DTA curves of raw pea pods, as well as KOH- and $ZnCl_2$-impregnated samples, are shown in Figure 5. Pyrolysis of raw pea pods involves four phases of deterioration. In the first phase, weight loss of around 4.15 percent is seen in the temperature range of 56.46 to 190 °C, which could be attributed to the release of water, such as moisture and bound water, as well as light volatile components. The second step shows a rapid decrease in the weight loss (approximately 44.07% at the temperature range from 192.98 to 275 °C), which could be attributed to depolymerization of hemicelluloses. The third step involves a gradual loss in weight at temperatures above 275 to 394.09 °C. However, there was a weight loss of 18.49%, which may be attributed to the decomposition of cellulose. The final step, which took place between 400 and 950 °C, showed a modest decreasing trend and a weight loss of 14.02 percent, which could be related to the degradation of the lignin moiety in pea pods as well as to the recombination of structure and synthesis of the fundamental carbon skeleton [62,63].

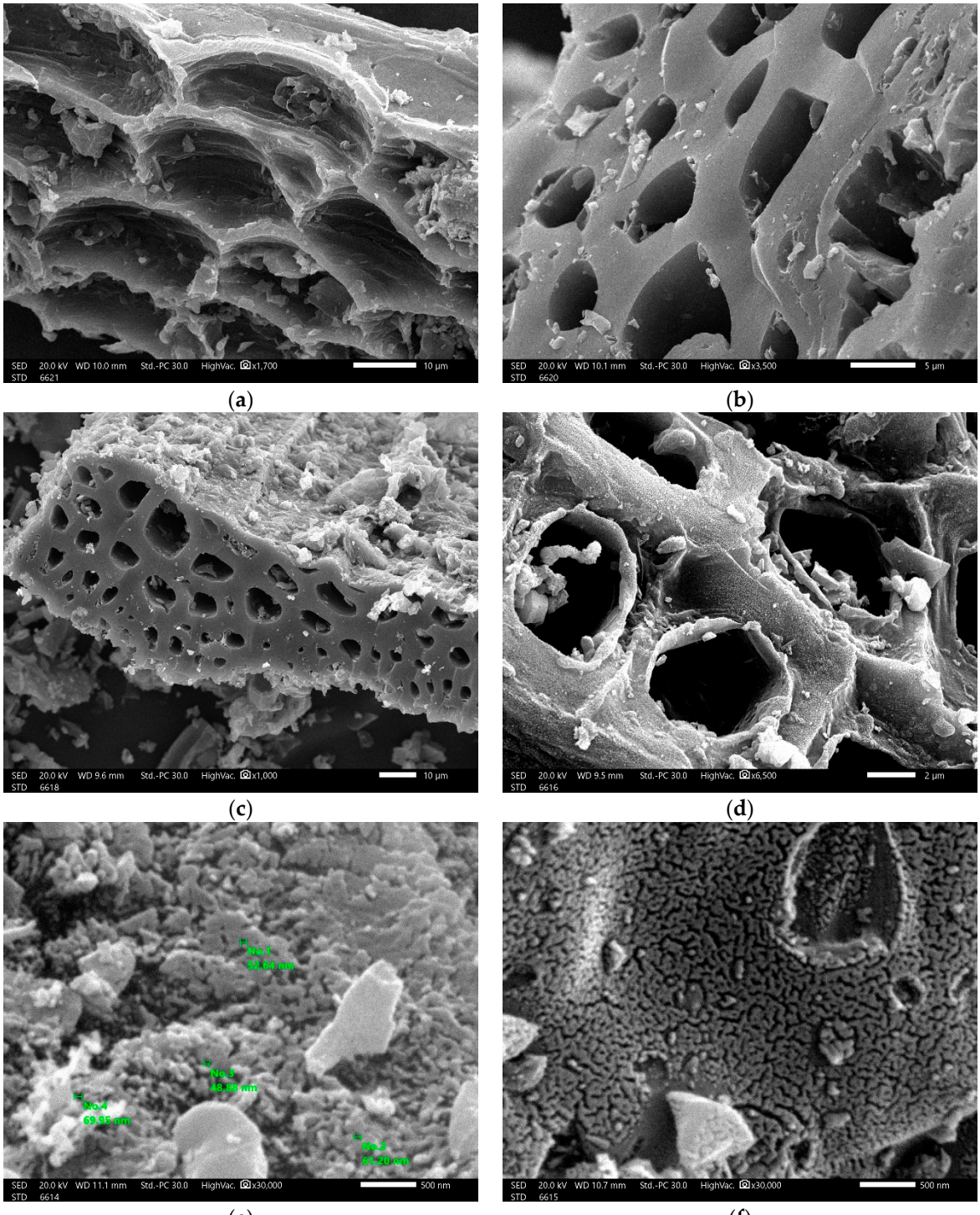

Figure 4. SEM image of pea pods/$ZnCl_2$/CO_2 (**a**,**b**) at 600 °C, (**c**,**d**) at 700 °C, (**e**,**f**) at 800 °C (SED 20.0 KV, Std.-PC 30.0 using high vacuum: max. (**a**) (×1700), (**b**) (×3500), (**c**) (×1000), (**d**) (×6500), (**e**), and (**f**) (×30,000).

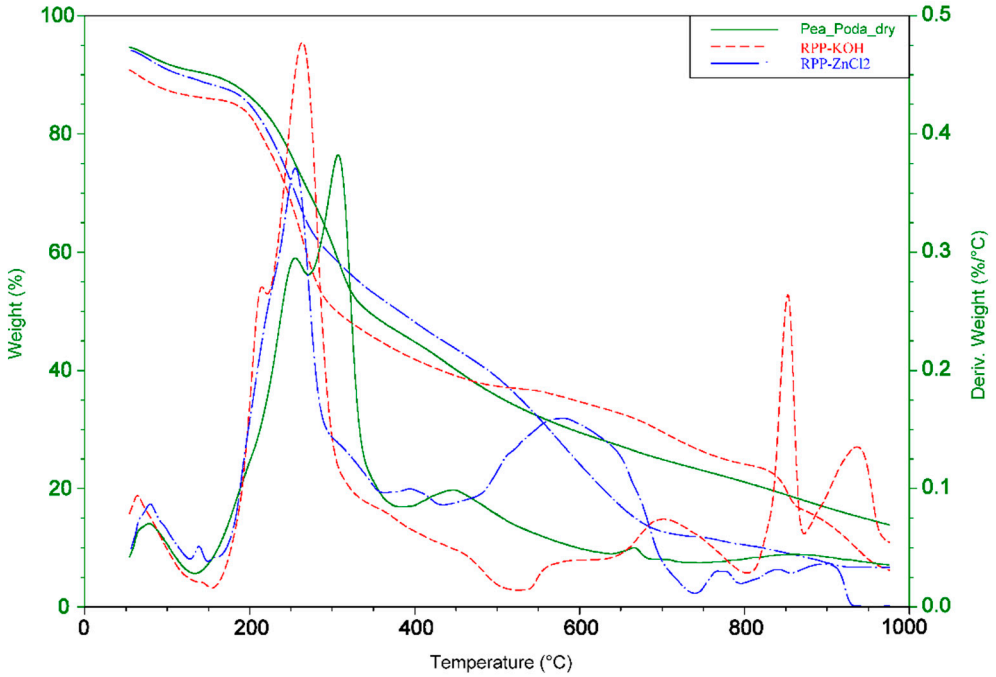

Figure 5. TGA and DTA of raw pea pods (green), pea pods + KOH (red), and pea pods + $ZnCl_2$ (blue) under temperatures from 50 to 1000 °C.

The DTA curve in Figure 5 shows a significant double maximum at 260 and 306.99 °C between 192.98 and 394.09 °C. This implies that the raw pea pods' primary breakdown took place in this temperature range. The TGA/DTA curves during the pyrolysis process at a 10% weight ratio of KOH impregnation are shown in Figure 5. During the pyrolysis process, KOH-impregnated samples show different thermal properties than raw pea pods, which could be owing to the reaction between pea pods and K compounds. The first step of weight loss was identical to raw pea pods and occurred at 55.86–160 °C, which is slightly sooner than raw pea pods (56.46–190 °C). Dehydration and moisture evaporation may be to blame for the weight loss [64]. The second weight loss happened between 183.51 and 541.59 °C, resulting in a 49.01 percent weight reduction. This weight loss is mostly due to the breakdown of activating agencies at temperatures about 200 °C, in which $KHCO_3$ rapidly degrades into H_2O and CO_2, resulting in increased weight loss [64] followed by hemicellulose and cellulose decomposition [65]. From 544–831 °C, the third weight loss of the KOH-impregnated sample occurred, with a small weight loss (12.84%), which can be attributed to the breakdown of K_2CO_3 and lignin [66]. The fourth weight loss of the KOH impregnated sample occurred at 831.70–950 °C, with a weight loss of 17.88%, which can be attributed to the ongoing degradation of lignin and K_2CO_3 as well as to the effect of burn-off at high temperatures, which causes the carbon skeleton to disintegrate.

It is worth noting that the mass continues to decrease from 700 to 950 °C due to the release of carbon dioxide and potassium sublimation [57]. This means that during the chemical activation of pea pods, the activation temperature should not exceed 800 °C. The largest rate of weight loss occurred at roughly 263.71, 699.96, and 852.36 °C, as seen in the DTG curve in Figure 5, and ended at around 986.95 °C. For $ZnCl_2$-activated sample, the pyrolysis process involved four steps, as shown in Figure 5. In the first stage, at around 58.84–130 °C, the $ZnCl_2$-activated sample experienced a weight loss of around 6.94%; this may be due to the released of H_2O within the biomass. The second and third stages showed more gradual reductions in mass (42.14 and 33.16%, respectively) from 178.18 to 745.02 °C. Meanwhile, a wide range of the weight loss was due to degradation process of lignocellulose materials and the release of moisture from the solid-phase $ZnCl_2$. The final stage showed a weight loss of 5.19% around 745.02–950 °C. The results were most likely of the total evaporation of the liquid phase from the $ZnCl_2$ at a temperature >700 °C. At temperatures

>800 °C, ZnO was reduced to metallic zinc [67]. The differential thermogravimetric analysis (DTA) of the $ZnCl_2$-activated sample shown in Figure 5 showed that the maximum weight loss rate was observed at two basic peaks at 254.99 °C and 588.24 °C.

2.2.5. Characterizations of Pore Structure

Different approaches (BET, t-Plot, MP, and BJH) were used to optimize the specific surface area of prepared activated carbons (Figures 6–10). The N_2 adsorption–desorption isotherms of activated carbon made from pea pods impregnated with 10% KOH and 2:1 $ZnCl_2$ for 1 h at various activation temperatures of 600, 700, and 800 °C under N_2 and CO_2 gases are shown in Figure 6a–d. In the comparison of the adsorption isotherms of different activated carbons, it is revealed in Figure 6 that the adsorption isotherms of the different activated carbons are typical type I microporous carbons according to IUPAC classification [22,23,68]. The nitrogen adsorption isotherm height of activated carbon (AC-KOH) at 800 °C is far more than that of activated carbon (AC-KOH) at 600 and 700 °C under N_2 gas (Figure 6a), while under CO_2 gas, the nitrogen adsorption isotherm height of activated carbon (AC-KOH) at 600 °C is far more than that of activated carbon (AC-KOH) at 700 and 800 °C (Figure 6b). Figure 6a, showing the AC-KOH samples at different temperatures from 600–800 °C under N_2, showed a small adsorption quantity compared to the AC-$ZnCl_2$ samples under the same conditions (Figure 6c). As illustrated in Figure 6b, the AC-KOH samples at 600, 700, and 800 °C in the presence of CO_2 exhibit a negligible capacity for N_2 adsorption compared to approximately one fourth of the AC-$ZnCl_2$ samples in the same conditions (Figure 6d). This finding reveals that when the impregnation reagent is changed from KOH to $ZnCl_2$, the porosity of activated carbon increases dramatically. As previously stated, Figure 6c,d demonstrates an increase in the maximum adsorption quantity when activated carbon made from pea pods soaked with 10% KOH is used (Figure 6a,b). However, the isotherms' knees are quite abrupt at low relative pressures (less than 0.05), and the adsorption capacity of samples (AC-$ZnCl_2$) for N_2 is close to saturation at 0.1. When the relative pressure is more than 0.1, the adsorption quantity increases very slowly. This implies that all samples activated with AC-$ZnCl_2$ possessed well-developed micropores. It is worth noting that a greater number of pores are formed in superficially modified activated carbon (AC-$ZnCl_2$) at 800 °C activation temperature under CO_2 gas than in other activated carbons (AC-$ZnCl_2$) at the same activation temperature under N_2 gas (AC-KOH) or at different activation temperatures from 600–800 °C under N_2 and CO_2 gases. We may conclude from the aforementioned data that the most effective parameter, among others, was the impregnation reagent ($ZnCl_2$) and the type of medium gas (CO_2).

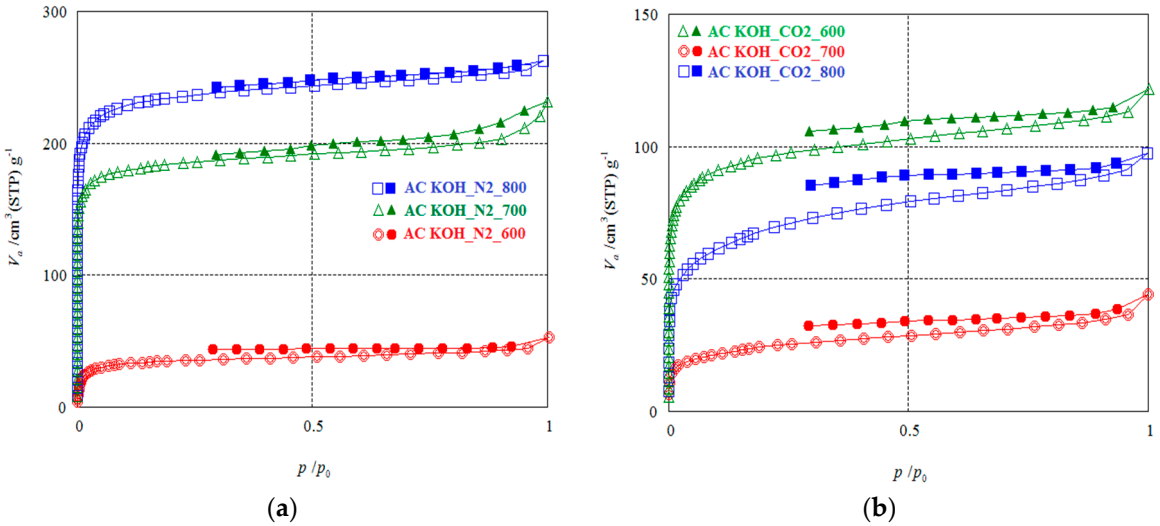

Figure 6. *Cont.*

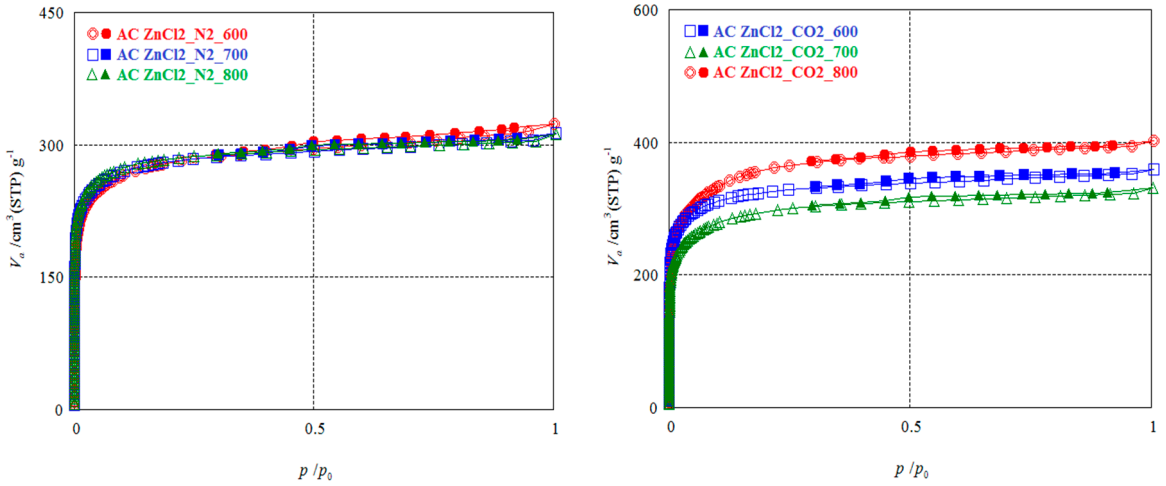

(**c**) (**d**)

Figure 6. (**a**) Adsorption/desorption of AC prepared from pea pods impregnated using (**a**) KOH and carbonized under N_2 gas flow, (**b**) KOH and carbonized under CO_2 gas flow, (**c**) $ZnCl_2$ and carbonized under N_2 gas flow, and (**d**) $ZnCl_2$ and carbonized under CO_2 gas flow.

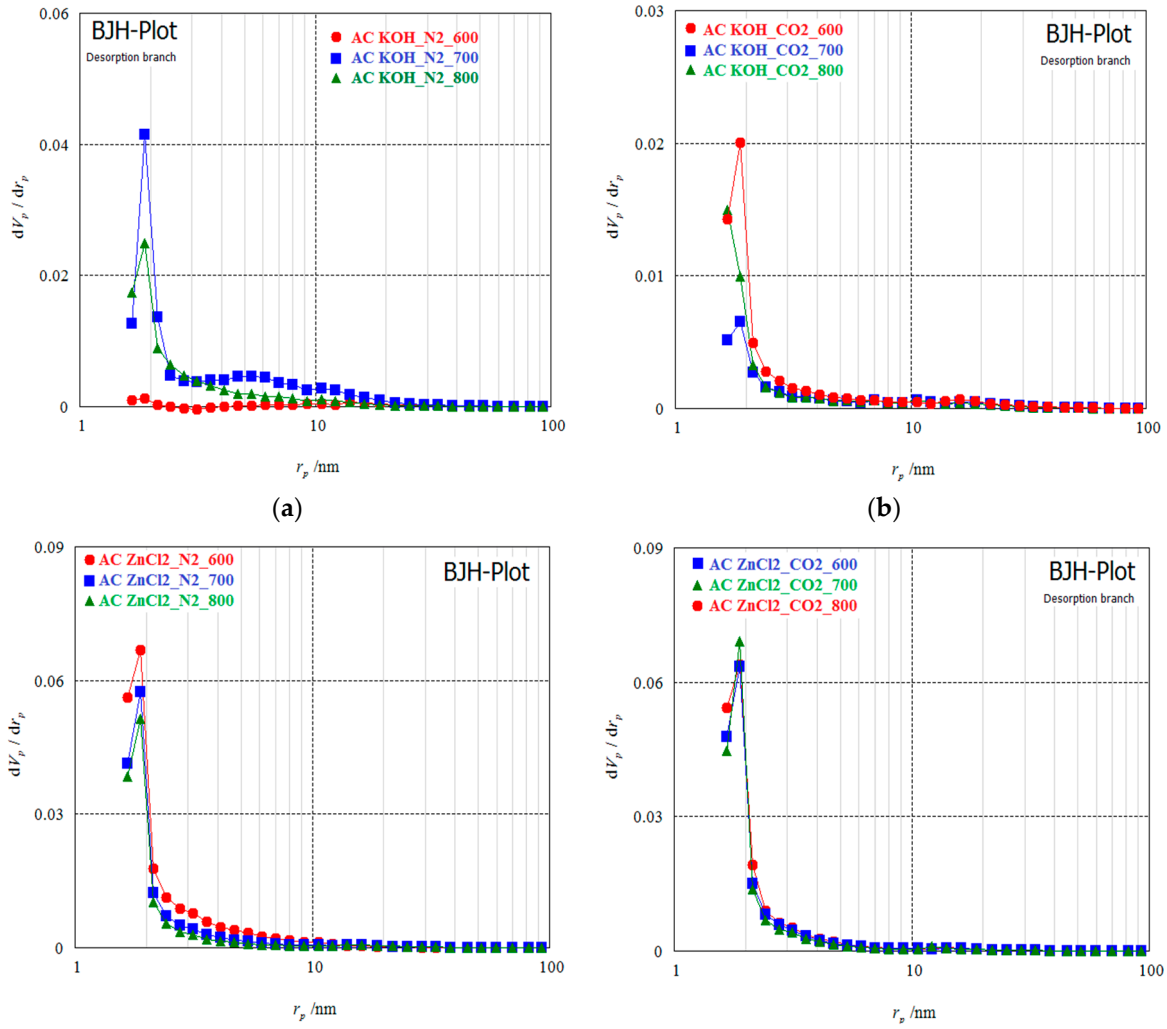

(**a**) (**b**)

(**c**) (**d**)

Figure 7. BJH analysis of AC prepared from pea pods impregnated using (**a**) KOH and carbonized under N_2 gas flow, (**b**) KOH and carbonized under CO_2 gas flow, (**c**) $ZnCl_2$ and carbonized under N_2 gas flow, and (**d**) $ZnCl_2$ and carbonized under CO_2 gas flow.

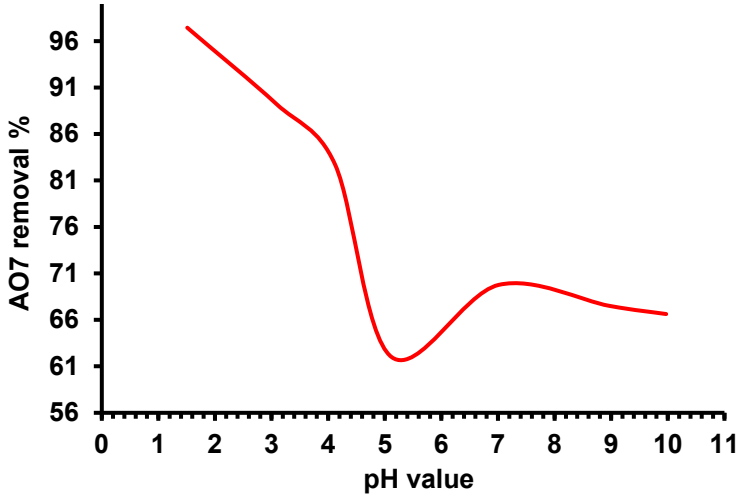

Figure 8. Effect of solution pH on the AO7 dye removal % using pea pods AC/$ZnCl_2$-800 °C under CO_2 (1.0 g/L) and 100 mg/L initial dye concentration at 25 ± 2 °C.

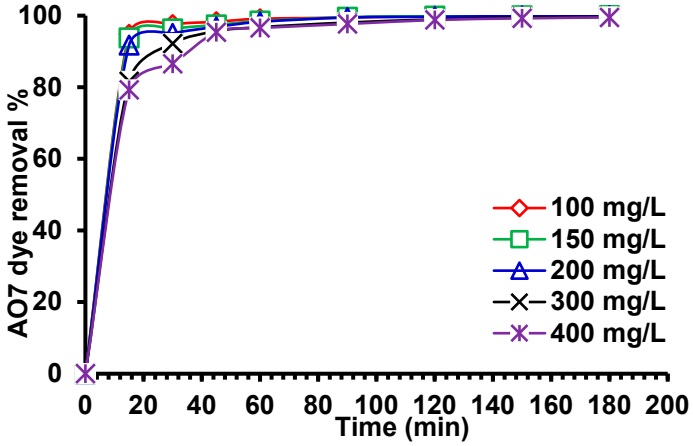

(**a**)

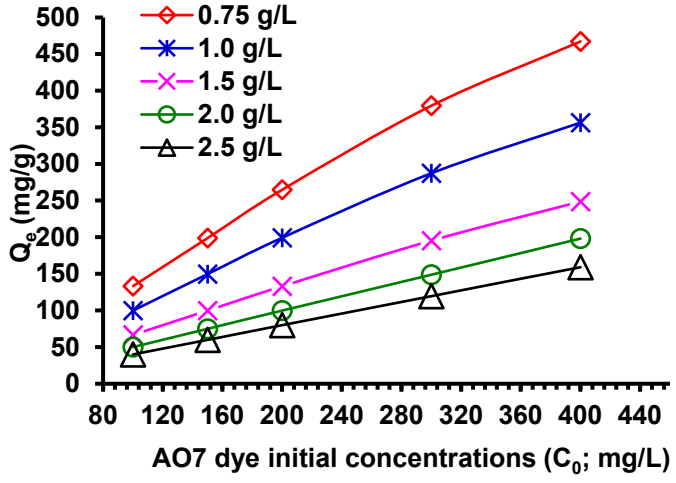

(**b**)

Figure 9. (**a**) Relation between removal % and contact time (min) of AO7 dye using different initial concentrations on 2.5 g/L of pea pods AC/$ZnCl_2$ at 25 ± 2 °C; (**b**) relation between Q_e (mg/g) and different initial concentrations (100–400 mg/L) of AO7 dye using different AC/$ZnCl_2$ (0.75–2.5 g/L) at 25 ± 2 °C.

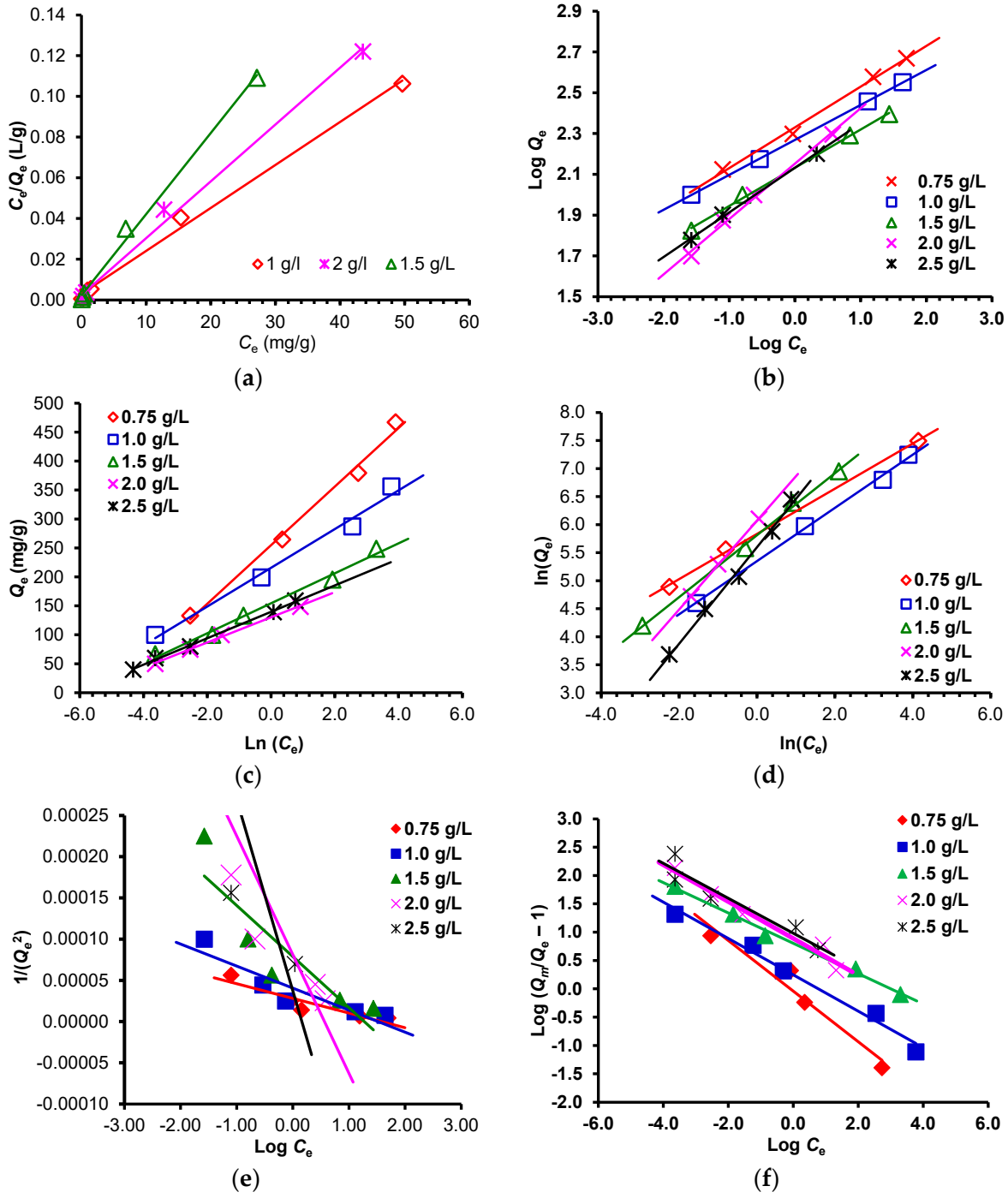

Figure 10. (**a**) Linearized Langmuir adsorption isotherm, (**b**) linearized Freundlich adsorption isotherm, (**c**) Tempkin adsorption isotherm, (**d**) Halsey adsorption isotherm, (**e**) Harkins–Jura isotherm, (**f**) generalized isotherm for AO7 dye of initial concentration (100–400 mg/L) on pea pods AC/$ZnCl_2$–800 °C under CO_2 doses at 25 ± 2 °C.

Table 1 lists the pore architectures of activated carbon generated from pea pod agricultural waste material using KOH and $ZnCl_2$ activation at 600–800 °C in the presence of N_2 and CO_2 gases. For impregnation of potassium-hydroxide-activated carbon (AC-KOH) under CO_2, the BET specific surface area was found to be 357.82, 87.70, and 241.84 m^2/g and the mean pore diameter was 2.068, 2.974, and 2.462 nm while the total pore volume was 0.185, 0.065 and 0.149 cm^3/g at 600, 700, and 800 °C, respectively. On the other hand, for impregnation of potassium-hydroxide-activated carbon under N_2, the BET specific surface

area (Figure S1) was found to be 197.33, 716.28, and 914.58 m^2/g and the mean pore diameter was 2.33, 1.94, and 1.77 nm while the total pore volume was 0.115, 0.347 and 0.405 cm^3/g at 600, 700, and 800 °C, respectively. Interestingly, when compared to CO_2, the AC-KOH exhibited greater improvements in specific surface area, mean pore diameter, total pore volume, and specific surface area per unit volume. These novel microporosity creations caused by the volatile evolution process, carbon oxidation process, and carbon gasification process may be responsible for this (AC-KOH, under N_2). During the chemical activation procedure for the samples of (AC-KOH) under CO_2, a widening of microporosity into the region of mesoporosity was observed. This could be due to the release of tar caused by the extreme activation of activated carbon, which resulted in an expansion of porosity in the activated carbon layer. When the temperature of activated carbon impregnated with $ZnCl_2$ (AC-$ZnCl_2$) was raised from 600 °C to 800 °C, the specific surface area of the activated carbon increased from 1039 m^2/g to 1084 m^2/g. Additional results revealed that when the temperature was raised from 600 to 800 °C, the total pore volume decreased somewhat, from 0.498 to 0.479 cm^3/g, and the microporosity was determined to be 1.915, 1805, and 1.767 nm in diameter. Clearly, the pore architectures of activated carbon impregnated with $ZnCl_2$ were significantly improved when exposed to CO_2.

As the temperature was raised from 600 to 800 degrees Celsius, the specific surface area increased dramatically, rising from 1228.00 to 1299.40 m^2/g as a result of the formation of a large number of new micropores. Additionally, when the temperature was raised from 600 to 800 °C, the total pore volume increased marginally, from 0.552 to 0.618 cm^3/g, despite the fact that the microporosity was 1.799, 1.859, and 1.901 nm. Finally, we conclude from these findings that activation with $ZnCl_2$ under both gas conditions resulted in a considerable and obvious improvement in pore architecture (Figure S1). Additionally, the t-plot approach (Figure S2) was used to determine the nitrogen adsorption isotherm, in which the adsorption amount is given as the thickness of the adsorption layer (*t*). In general, t-plots can be classified into three types. However, this classification is arbitrary, as there is no type established by the IUPAC as there is with adsorption isotherms. However, as seen in Figure 8, the t-plot has two distinct slopes, one of which is a steep slope going through the initial point and the other of which is a more gradual slope, indicating that the adsorbent has micropores of uniform size. The amount of adsorption grows dramatically during the early stages of adsorption due to adsorption into micropores, while the thickness of adsorption does not increase as much. Once adsorption into micropores is complete, no further adsorption occurs on the surface.

As shown in Table 1, the pore surface area and volume were somewhat different than those determined by BET; this result suggested that the maximum specific surface area of micropores is expected to be between 1300 and 1500 m^2/g. It is worth noting that the average pore diameter (2t) was significantly different than that determined by BET. Generally, the value (2t) produces incorrect analysis findings if the pore size is more than two layers. Additionally, when the 2t value is less than 0.7 nm, as it is with micropore filing, one can obtain an approximate indication of the size of the pores, but there is no numerical value to rely on. Because the MP-plot (Figure S3) is a derivation of the t-plot, the MP-plot's results closely match those of the t-plot.

The mesopore and micropore size distributions of activated carbons generated by KOH at various activation temperatures (600, 700, and 800 °C) in the presence of N_2 and CO_2 are depicted in Figure 9a,b, respectively. Under N_2 rather than CO_2, activated carbons (AC-KOH) are dominated by micropores, and all activated carbons have a distribution peak about 0.6 nm.

As illustrated in Figure S3a, the samples (AC-KOH) at 700 and 800 °C have a similar number of micropores, whereas the samples (AC-KOH) at 600 °C have fewer micropores. This demonstrates that changing the activation temperature has a significant effect on micropore formation. In comparison, Figure S3b demonstrates that the sample (AC-KOH) heated to 600 °C under CO_2 has a greater number of micropores than the samples (AC-KOH) heated to 700 and 800 °C. This suggests that switching to CO_2 as the gas medium has

a detrimental influence on the formation of micropores. The micropore size distributions of activated carbons generated with $ZnCl_2$ at various activation temperatures (600, 700, and 800 °C) in the presence of N_2 and CO_2 are shown in Figure 9c,d. As shown in Figure S3c, all activated carbon samples (AC-$ZnCl_2$) have micropore sizes ranging from 0.4 to 1.1 nm and a distribution peak at 0.6 nm. We must emphasize that all samples (AC-$ZnCl_2$) produced in N_2 exhibit nearly identical micropores. As shown in Figure S3d, a similar trend is observed for (AC-$ZnCl_2$) under CO_2, with the sample (AC-$ZnCl_2$) at 600 °C having more developed micropores than the samples (AC-ZnC_2) at 700 and 800 °C, indicating that the micropores developed more with a decrease in the activation temperature and using CO_2 gas as an activation reagent. According to Figure 7a, all samples of (AC-KOH) under N_2 had micropores with a radius of 2 to 3 nm and a distribution peak near 2.5 nm. At 600, 700, and 800 °C, the integrated pore volume (*V*p) was 0.0189, 0.0724, and 0.0376 $cm^3\ g^{-1}$, respectively (Table 1). The pore size distribution of (AC-KOH) produced under CO_2 is between 2 and 4.5 nm, with distribution peaks around 2.5 nm (Figure 7b). At 600, 700, and 800 °C, the integrated pore volume (*V*p) was 0.0280, 0.0190, and 0.0199 $cm^3\ g^{-1}$, respectively (Table 1). According to Figure 7c, all samples of (AC-$ZnCl_2$) in N_2 had micropores with a radius of 1.5 to 2.5 nm and a distribution peak around 2 nm. At 600, 700, and 800 °C, the integrated pore volume (*V*p) was 0.0690, 0.0495, and 0.0433 $cm^3\ g^{-1}$, respectively (Table 1). All (AC-$ZnCl_2$) produced under CO_2 had pore sizes ranging from 1 to 2.5 nm, with distribution peaks around 2 nm (Figure 7d). At 600, 700, and 800 °C, the integrated pore volume (Vp) was 0.0529, 0.0516, and 0.0581 $cm^3\ g^{-1}$, respectively (Table 1). It appears from this result that the pore size of (AC-$ZnCl_2$) generated under CO_2 and N_2 conditions can give a large specific surface area, making it well-suited for the adsorption and removal of pollutants from water and wastewater.

2.3. Acid Orange 7 Dye Adsorption Study

The selective activated carbon soaked with 2:1 $ZnCl_2$ and heated to 800 °C in the presence of CO_2 gas was utilized as an adsorbent to remove AO7 dye from water based on a general test comparing all the manufactured activated carbons under various conditions. The effects of pH, contact time, initial dye solution concentration, and adsorbent dose at room temperature were explored in order to design viable wastewater adsorption systems. Adsorption isotherms and kinetic models were also investigated in this study.

2.3.1. Effect of Solution pH on the Adsorption Process

In the absorption process, the pH of a solution is believed to be a significant parameter for predicting the adsorption of dyes onto adsorbents during the adsorption procedure. In part, this is because the acidity or alkalinity (pH) of the solution has an effect on its chemistry and, subsequently, on the interaction between its functional group and the dye. The effect of solution pH on AO7 dye removal was investigated using a 100 mg/L initial dye concentration and pea pod activated carbon (AC-$ZnCl_2$) prepared at 800 °C under CO_2 gas (1.0 g/L) as an adsorbent, with the pH of the solution being varied from 1 to 11 at room temperature (Figure 8). Figure 8 shows that AO7 dye removal efficiency decreased as the pH increased; however, when the pH of the solution reached 5.12, the removal of dye started to increase slightly until pH 7 and then started to decrease again. The maximum percentage uptake was obtained at pH 1.51 (97.4%), while the uptake percentage of AO7 dye at pH 5.12 and 9.97 had the minimum values (62.0 and 66.6%, respectively). It appears that the changing of pH value led to the formation of a different carbon surface charge. In particular, at lower pH values, protonation onto the surface of the adsorbent occurred. It is worth noting that the activated carbon (AC-$ZnCl_2$) was indeed essentially microporous and had a higher surface area, implying that their overall porosity was available for dye adsorption because the activated carbon (AC-$ZnCl_2$) allowed H^+ ions to enter the micropores structure, forming strong electrostatic attraction between negatively charged AO7 dye anions and positively charged adsorption sites and resulting in an increase in adsorption efficiency.

2.3.2. Impact of Contact Time and Initial Dye Concentration on the Adsorption Process

Finally, the adsorption capacity is highly dependent on the time of adsorption. Thus, the time course of the percentage removal of AO7 dye adsorbed on the AC-$ZnCl_2$ (2.5 g/L) was investigated using AO7 dye at various starting concentrations (100–400 mg/L) at ambient temperature (Figure 9a). At an early stage (15 min), the percentage of AO7 dye removed increased rapidly and the initial adsorption rate onto the activated carbon surface via the interconnected micropores was extremely high—on the order of 94.76, 93.75, 91.75, 81.61, and 79.24 percent for initial concentrations of 100, 150, 200, 300, and 400 mg/L, respectively (Figure 9a). Additionally, notice that prior to reaching equilibrium (15–60 min), there is a small increase in AO7 dye removal efficiency with increasing contact time. After approximately 60 min, equilibrium adsorption was achieved for all initial dye concentrations (100–400 mg/L), with removal percentages of 99.11, 98.46, 98.24, 96.77, and 96.53%, respectively, and the maximum percentage removal of dye (100 percent) was observed after 180 min for all initial concentrations (Figure 9a). The initial concentration acts as a powerful motivator for overcoming mass transfer resistances between the solid surface and liquid phase. The relationship between starting dye concentrations of 100–400 mg/L, different adsorbent dosages of AC-$ZnCl_2$ (0.75–2.5 g/L), and adsorbent quantity (Q_e) was examined. The investigation's findings are depicted in Figure 9b.

The quantity of adsorbent of AO7 dye at equilibrium (Q_e) increases from 133.23 to 467.16 mg/g with increasing starting concentrations from 100 to 400 mg/L in the current investigation at adsorbent dosage 0.75 g/L. With an increase in the starting concentration from 100 to 400 mg/L, the quantity of adsorbent of AO7 dye at equilibrium (Q_e) increased from 99.97 to 356.47, 66.65 to 248.58, 49.94 to 198.13, and 39.99 to 159.15 mg/g at adsorbent dosages of 1.0, 1.5, 2.0, and 2.5 g/L of AC-$ZnCl_2$, respectively. With a decrease in the adsorbent doses from 0.75 to 2.5 g/L, the Q_e increased dramatically from 159.15 to 467.16 mg/g at an initial concentration of 400 mg/L. It is widely assumed that the mechanism for dye adsorption is linked to the pore structures of activated carbon, specifically activated carbon prepared by $ZnCl_2$ and CO_2 activation, which showed the ability to exhibit a large number of micropores and a large quantity of oxygen-containing functionalities of C−O groups in carboxylic acids, alcohols, phenols, ethers, esters, or the P=O bond in phosphate esters, which can provide active sites for dyes (Figures 2 and 3).

2.3.3. Adsorption Isotherms

To describe adsorption mechanisms, adsorbate interaction with adsorbent, and adsorbate distribution between the liquid and solid phases at equilibrium, five isotherm equations were fitted to the experimental data. The adsorption of AO7 dye onto AC-$ZnCl_2$ was examined using the Langmuir, Freundlich, Harkins–Jura, Halsey, generalized, and Tempkin isotherm models [69]. The slopes, intercepts, and correlation coefficients (R^2) were used to derive the isotherm model parameters, which are listed in Table 2. Based on the Langmuir constant, K_L and R^2 were both larger at the higher adsorbent dose (2.5 g/L), indicating a stronger interaction between the adsorbent and adsorbate. The Langmuir isotherm equation was found to be the best fit for the adsorption equilibrium data of the activated carbon (AC-$ZnCl_2$) sample, with the highest R^2 value being ~1.000, implying that this isotherm provides the most accurate representation of the experiment data and indicating the homogeneous nature of activated carbon. The findings also showed that monolayer physical adsorption could effectively explain the adsorption of AO7 dye onto activated carbon from aqueous solutions and that adsorbate molecules on the surface of the AC-$ZnCl_2$ are energetically equal. Furthermore, the quantity of adsorption equivalent to complete monolayer coverage calculated using the Langmuir model (Q_m) was 473.93 mg/g, which is extremely close to the 467.16 mg/g observed from practical measurements at 0.75 g/L (Table 2).

These results can be explained as follows: the carbon activated by $ZnCl_2$ under CO_2 at 800 °C, which has the largest surface area (1300 to 1500 m^2/g) and highest total pore volume (0.6176 cm^3/g) (Table 1) and also showed the highest adsorption capacity (467.16 mg/g) of

AO7 dye, had an excellent fit with the Langmuir isotherm due to the predominant presence of micropores with small diameters, which provided more channels and binding sites for AO7 dye onto the surface of the adsorbent and more difficulty for the penetration of AO7 dye ions as a bulk component, indicating the occurrence of physical adsorption. In addition, there were more aromatic C=C groups in the activated carbon (AC-$ZnCl_2$) prepared under CO_2 activation than that prepared under N_2, and the π–π dispersion interaction between the aromatic structures of AO7 dye and AC-$ZnCl_2$ prepared under CO_2 activation can also increase the adsorption performance (Figure 2d).

Table 2. Isotherm study results of AO7 dye adsorption at room temperature (25 ± 2 °C) onto activated carbon generated at 800 °C carbonization temperature under CO_2 using $ZnCl_2$ as the activating agent (AC-$ZnCl_2$) at varying initial concentrations (100–400 mg/L).

Isotherm Model	Isotherm Parameter	Pea Pod Activated Carbon (g/L)				
		0.75	**1.00**	**1.50**	**2.00**	**2.50**
Langmuir	Q_m (mg/g)	473.93	250.00	358.42	153.61	124.22
	$K_L \times 10^3$	0.70	1.74	1.12	12.06	23.68
	R^2	0.996	0.996	0.995	1.000	1.000
Freundlich	$1/n$	0.200	0.172	0.187	0.272	0.219
	K_F ($mg^{1-1/n}L^{1/n}g^{-1}$)	214.24	185.99	135.74	142.33	135.74
	R^2	0.995	1.000	0.998	0.992	0.998
Harkins–Jura isotherm	A_{HJ}	50,000	33,333	16,667	10,000	5000
	B_{HJ}	1.50	1.33	1.33	0.80	0.20
	R^2	0.857	0.843	0.795	0.788	0.523
Halsey isotherm	$1/n_H$	5.09	5.95	5.41	5.23	4.02
	K_H	2.87	2.42	2.49	2.52	3.34
	R^2	0.995	0.989	0.981	0.977	0.897
Tempkin	A_T	142.28	634.62	390.58	409.81	460.75
	B_T	50.60	33.45	25.90	21.67	22.81
	b_T	48.96	74.07	95.67	114.36	108.64
	R^2	0.992	0.987	0.989	0.997	0.998
Generalized isotherm	N_b	0.45	0.32	0.27	0.33	0.31
	K_G	0.91	1.77	6.38	7.78	9.58
	R^2	0.949	0.982	0.993	0.968	0.913

2.3.4. Adsorption Kinetics

The rate kinetics of the AO7 dye adsorption on the activated carbon AC-$ZnCl_2$ in relation to residence time was examined to regulate and understand the adsorption dynamic mechanisms and solute absorption at the solid–solution interface, including the diffusion process. The models used were pseudo-first-order, pseudo-second-order, Elovich, intraparticle, and film diffusion. The correlation coefficient was used to express the similarity of experimental and model-predicted data (R^2).

The Pseudo-First-Order and Pseudo-Second-Order Kinetic Models

The kinetic data for AO7 dye adsorption at various initial dye concentrations (100–400 mg/L) and varied adsorbent dosages of AC-$ZnCl_2$ (0.75–2.5 g/L) were calculated from the associated plots and are summarized in Table 3. Figure 11a,b illustrates the graphs of The pseudo-first-order and pseudo-second-order kinetic models, respectively. According to the results, the correlation coefficients for the pseudo-second-order kinetic model (1.000) were significantly higher than those for the pseudo-first-order kinetic model; secondly, increasing the initial dye concentration from 100 to 400 mg/L at 0.75 g/L results in an increase in the calculated Q_e values from 138.89 to 500.00 mg/g. Finally, because the experimental adsorption capacity (467.16 mg/g) was nearly identical to that predicted by the pseudo-second-order kinetic model (500.00 g/L), it was concluded that the studied adsorption system obeys the pseudo-second-order kinetic model and that physisorption may be the rate-limiting step [69].

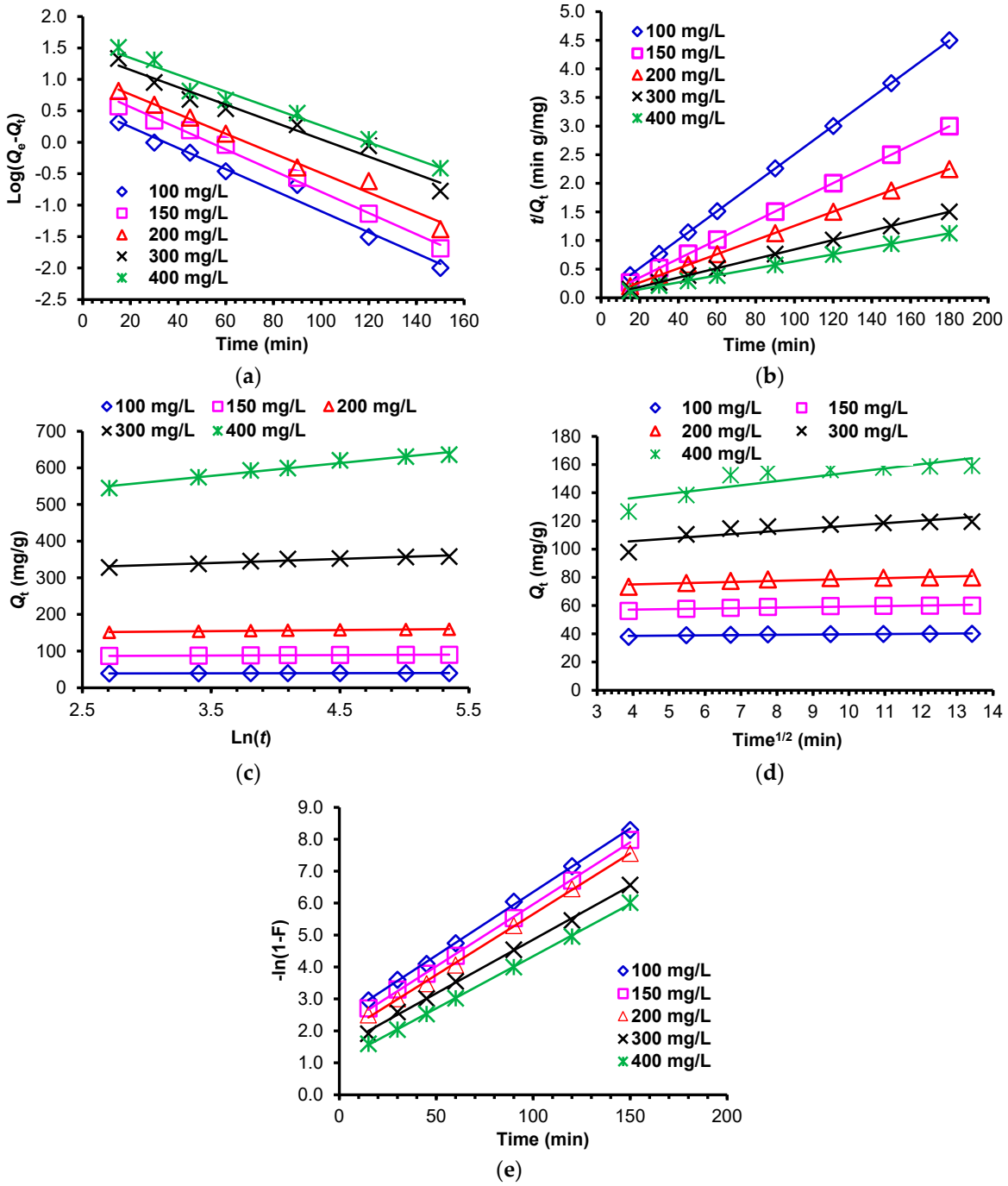

Figure 11. (**a**) Pseudo-first-order kinetic, (**b**) pseudo-second-order kinetic, (**c**) Elovich kinetic, (**d**) intra-particle diffusion, (**e**) film diffusion of adsorption of AO7 dye of initial concentration (100–400 mg/L) by pea pod AC/$ZnCl_2$–800 °C under CO_2 dose (2.5 g/L) at 25 ± 2 °C.

Elovich Kinetic Model

This model is frequently used to describe the chemisorption mechanism, which may be responsible for controlling the rate of adsorption. Figure 11c illustrates the Elovich kinetic data obtained in this investigation for the adsorption of AO7 dye starting concentrations (100–400 mg/L) at adsorbent doses (2.5 g/L) from aqueous solution at room temperature onto AC-$ZnCl_2$. The linear connection depicted in Figure 11c has a slope of $1/\beta$ and an intercept of $1/\beta \ln(\alpha\beta)$ (Equation (15)). The desorption constant (β), the initial adsorption rate constant (α), and the correlation coefficient (R^2) are shown in Table 4 and are all derived from the Elovich rate Equation (15). Despite the fact that the desorption constant

(β) dropped when the initial concentrations of AO7 dye increased from 100 to 400 mg/L and the initial adsorption rate (α) increased, the correlation coefficient (R^2) is lower than that predicted by the intraparticle and film diffusion kinetic models. This result shows that the Elovich model was not the best model.

Intraparticle and Film Diffusion Kinetic Models

Additionally, to investigate the likelihood of dye ion molecules being transferred from the bulk solution into the pores or onto the adsorbent's outer surface via film diffusion or intraparticle diffusion, the rate-limiting stage in the adsorption process was used. In essence, the slower of the two steps will serve as the rate-limiting step. The intraparticle and film diffusion rate constants (K_{dif} and K_{FD}, respectively) and correlation coefficient (R^2) calculated from the intraparticle and film diffusion rate equations are listed in Table 4. Figure 11d,e illustrates the intraparticle and film diffusions of AO7 dye at starting concentrations (100–400 mg/L) and adsorbent doses (2.5 g/L) onto AC-$ZnCl_2$. As illustrated in Figure 11d,e, the plots in both models are linear and do not pass through the origin.

As shown in Table 3, the correlation coefficient (R^2) was 1.000 for all initial concentrations of AO7 dye (100–400 mg/L) at various adsorbent dosages (0.75–2.5 g/L) of AC-$ZnCl_2$) in the film diffusion model. However, the correlation coefficient (R^2) was lower in the intraparticle diffusion model. According to the results, the film diffusion technique was used to modulate the adsorption rate of AO7 dye ions onto the AC-$ZnCl_2$. The linear deviation from the origin or near saturation during the adsorption process could be due to the presence of an initial boundary layer of H^+ ions that penetrated the micropore and act as a barrier to the intraparticle diffusion mechanism, or it could be due to the difference in mass transfer rates between the initial and final stages of adsorption [70,71].

Table 3. The findings of pseudo-first-order and pseudo-second-order adsorption of AO7 dye at various initial concentrations (100–400 mg/L) at 25 ± 2 °C onto pea pod activated carbon generated at a carbonization temperature of 800 degrees Celsius in the presence of CO_2 using $ZnCl_2$ as the activating agent.

Parameter			First-Order Kinetic Model			Second-Order Kinetic Model			
AC (g/L)	AO7 Dye (mg L^{-1})	q_e (exp.)	q_e (calc.)	$k_1 \times 10^3$	R^2	q_e (calc.)	$k_2 \times 10^3$	h	R^2
0.75	100	133.23	101.81	46.52	0.989	138.89	0.99	19	1.000
	150	198.77	144.18	38.69	0.992	212.77	0.48	22	0.999
	200	264.77	185.65	28.79	0.898	285.71	2.68	219	0.999
	300	379.51	195.48	24.87	0.988	400.00	0.22	36	1.000
	400	467.16	223.87	19.81	0.963	500.00	0.15	38	0.999
1.0	100	99.97	36.53	39.61	0.981	103.09	2.26	24	1.000
	150	149.71	64.46	37.77	0.968	156.25	1.05	26	1.000
	200	199.26	81.49	22.80	0.853	208.33	0.50	22	1.000
	300	287.24	122.01	21.88	0.994	303.03	0.32	29	1.000
	400	356.47	138.90	16.81	0.967	370.37	0.24	33	0.999
1.5	100	66.65	22.09	47.44	0.969	68.03	4.89	23	1.000
	150	99.89	47.40	46.29	0.995	103.09	2.09	22	1.000
	200	133.05	47.96	34.08	0.971	136.99	1.37	26	1.000
	300	195.44	87.24	25.56	0.912	204.08	0.58	24	0.999
	400	248.58	96.32	21.88	0.974	263.16	3.80	263	1.000
2.0	100	49.99	10.20	43.07	0.965	50.76	9.88	25	1.000
	150	74.96	17.96	42.38	0.974	76.34	4.82	28	1.000
	200	99.89	27.52	37.08	0.927	102.04	2.61	27	1.000
	300	148.75	50.69	31.78	0.965	153.85	1.24	29	1.000
	400	198.13	84.94	27.18	0.979	208.33	0.61	26	1.000
2.5	100	39.99	3.79	38.69	0.981	40.16	26.72	43	1.000
	150	59.99	7.92	38.92	0.995	60.61	12.43	46	1.000
	200	79.97	11.87	35.93	0.986	80.65	7.39	48	1.000
	300	119.57	26.85	31.78	0.968	121.95	2.62	39	1.000
	400	159.15	40.96	31.09	0.970	163.93	1.50	40	1.000

Table 4. The results of Elovich, intraparticle diffusion, and film diffusion kinetic models used to predict the adsorption of AO7 dye (100–400 mg/L) onto pea pod activated carbon produced at 800 °C carbonization temperature under CO_2 using $ZnCl_2$ as the activating agent.

AC (g/L)	AO7 conc.	Elovich			Interaparticle Diffusion			Film Diffusion		
		β	α	R^2	K_{dif}	C	R^2	K_{FD}	C	R^2
0.75	100	0.0542	2.23×10^2	0.927	0.15	1.82	0.887	0.05	0.44	1.000
	150	0.0322	1.55×10^2	0.960	0.17	1.93	0.927	0.04	0.47	0.999
	200	0.0245	1.75×10^2	0.993	0.18	2.03	0.982	0.33	0.41	0.999
	300	0.0179	3.44×10^2	0.990	0.17	2.21	0.975	0.26	0.63	0.999
	400	0.0143	1.42×10^1	0.977	0.18	2.27	0.971	0.21	0.68	1.000
1.0	100	0.1067	3.60×10^3	0.906	0.09	1.80	0.871	0.04	1.03	0.999
	150	0.0525	4.46×10^2	0.884	0.13	1.90	0.846	0.04	0.67	1.000
	200	0.0356	2.51×10^2	0.974	0.16	1.96	0.951	0.03	0.67	0.997
	300	0.0250	3.61×10^2	0.982	0.16	2.11	0.966	0.02	0.84	0.997
	400	0.0213	5.22×10^2	0.968	0.16	2.20	0.969	0.02	0.82	0.999
1.5	100	0.1972	2.43×10^4	0.869	0.07	1.67	0.831	0.05	1.07	0.996
	150	0.0966	1.47×10^3	0.889	0.10	1.78	0.851	0.05	0.80	0.999
	200	0.0668	9.62×10^2	0.891	0.12	1.88	0.855	0.04	0.82	0.998
	300	0.0456	1.04×10^3	0.988	0.13	2.02	0.978	0.03	0.76	0.995
	400	0.0295	3.76×10^2	0.974	0.15	2.07	0.950	0.03	0.55	0.999
2.0	100	0.4188	2.66×10^7	0.892	0.05	1.60	0.864	0.05	1.50	0.999
	150	0.2040	1.97×10^5	0.873	0.06	1.74	0.843	0.04	1.40	0.998
	200	0.1111	5.47×10^3	0.874	0.09	1.81	0.837	0.04	0.85	0.998
	300	0.0643	1.87×10^3	0.901	0.11	1.94	0.872	0.03	0.90	0.997
	400	0.0434	8.93×10^2	0.975	0.13	2.02	0.960	0.03	0.83	0.998
2.5	100	1.1502	7.05×10^{17}	0.921	0.02	1.56	0.897	0.04	2.37	0.999
	150	0.6039	7.34×10^{13}	0.969	0.03	1.72	0.947	0.04	2.08	0.999
	200	0.3456	2.43×10^{10}	0.955	0.03	1.83	0.932	0.04	1.85	0.999
	300	0.1163	8.26×10^4	0.863	0.07	1.93	0.828	0.03	1.50	0.999
	400	0.0714	1.05×10^4	0.885	0.09	2.02	0.856	0.03	1.07	1.000

2.3.5. Adsorption Mechanism

As previously stated, the adsorption mechanism of the AO7 dye onto the AC-$ZnCl_2$ surface can be extrapolated from pore structure studies, FTIR, adsorption isotherms, and kinetics model results. To begin, the presence of a large number of new micropores enhanced the diffusion of the H^+ ions, forming the film via electrostatic attraction caused by functional groups such as C−H (aldehydes), C−O group in carboxylic acids, alcohols, phenols, ethers, and esters, or the P=O bond in phosphate esters. Secondly, the π–π interactions that occur between the π–electron system (C=C skeletal stretching of the aromatic rings) of the AC-$ZnCl_2$ structure, and the aromatic rings of the AO7 dye molecules did the same (Figure 12).

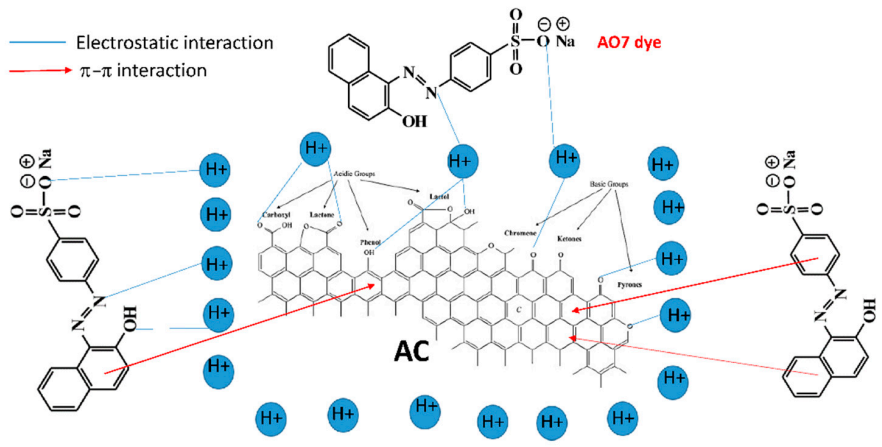

Figure 12. Shows the possible adsorption mechanisms of the adsorption of AO7 dye onto the microporous surface of activated carbon (AC-$ZnCl_2$) produced at 800 °C under CO_2 gas through electrostatic interaction and π–π interaction.

2.3.6. Comparison of the Q_m of AO7 Dye onto Different ACs

Table 5 compares the maximum adsorption capacity (Q_m) of several types of adsorbents employed to remove AO7 dye from its aqueous solution to the present work. When compared to other adsorbents reported in the literature, the *Pisum sativum* pea pod AC-$ZnCl_2$ demonstrated a greater affinity for AO7 dye removal, with a Q_m of 473.93 mg/g (Table 5). The increased adsorption capacity of AC-$ZnCl_2$ may be a result of the micropores produced on its surface. As a result, AC-$ZnCl_2$ derived from pea pod solid waste can be employed as a promising adsorbent for extracting AO7 dye from wastewater.

Table 5. Comparative study of the adsorption capability of AO7 dye on various adsorbents.

Adsorbent	Adsorption Capacity (mg/g)	Reference
Pisum sativum pea pod AC-$ZnCl_2$	473.93	This work
Brown coal fly ash	82.8	[72]
Chemically treated wood shavings	179.7	[73]
Oxihumolite	50.0	[74]
Commercial granular activated carbon	40.0	[75]
Euphorbia macroclada	455.0	[76]
Casuarina wood activated carbon	7.80	[77]
Biochar (pea *Pisum sativum* peel)	523.12	[14]

2.3.7. Desorption Studies

The desorption study of desorbed AO7 dye on AC-$ZnCl_2$ was carried out by using 1% NaOH (w/v). It was found that the AC-$ZnCl_2$ can be used as an adsorbent for more than six cycles without much change in adsorption efficiency. The amount of desorbed AO7 dye was determined by using the following Equation (1):

$$Q_d = \frac{(C_d - C_s)V}{W} \quad (1)$$

where C_d is concentration of AO7 dye after desorption and C_s is concentration of dye after adsorption. The results of adsorption and desorption cycles are represented in Figure 13.

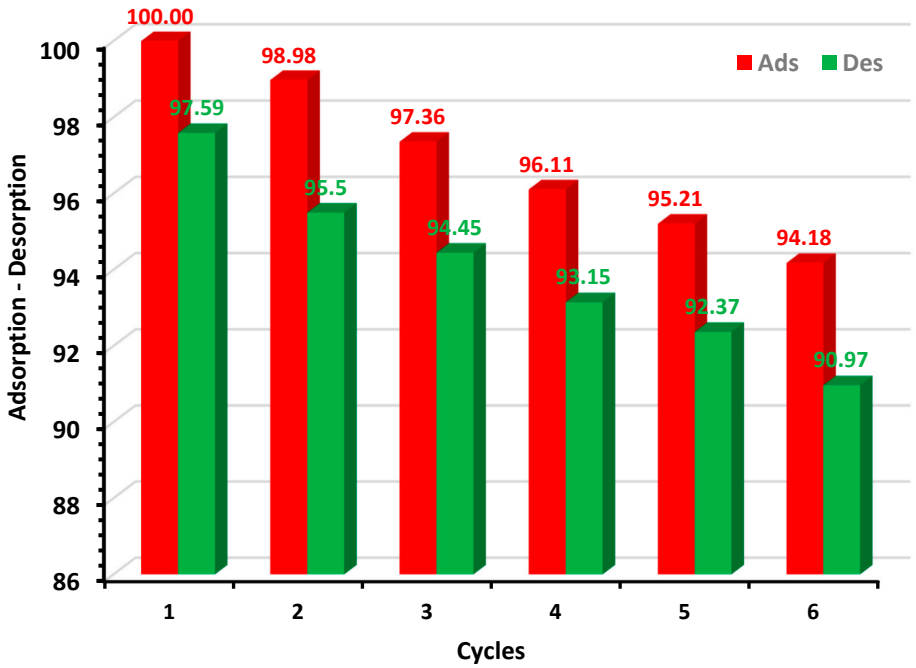

Figure 13. Adsorption–desorption studies for AC-$ZnCl_2$ recycle studies.

2.4. Optimization Study

The design matrix was used to investigate the interaction effects of three important factors, including contact time, activated carbon dose, and initial AO7 dye concentration on the removal of AO7 dye. The experimental design and the responses are shown in Table 6. Based on the obtained results, the following polynomial Equations (2) and (3) for AO7 dye removal were developed:

$$\text{Removal \% for Coded Factors} = 94.79 + 10.51A + 7.25B - 5.69C - 2.99AB + 1.56AC + 2.7BC - 7.13A^2 - 3.3B^2 - 0.1193C^2 \quad (2)$$

$$\text{Removal \% for Actual Factors} = 58.32749 + 0.605691\ \text{Time} + 21.57175\ \text{Dose} - 0.082057\ \text{Conc.} - 0.065112\ \text{Time} \times \text{Dose} + 0.000198\ \text{Time} \times \text{Conc.} + 0.020565\ \text{Dose} \times \text{Conc.} - 0.002585\text{Time}^2 - 4.31590\ \text{Dose}^2 - 0.000053\ \text{Conc.}^2 \quad (3)$$

Table 6. Experimental design for adsorption of AO7 dye on activated carbon.

	Independent Factors			Response %	
Run	**Time (A)**	**Dosage (B)**	**Concentration (C)**	**Experiment**	**Predicted**
1	120	0.75	400	82.88	83.66
2	15	2.0	100	89.63	86.91
3	15	2.5	400	79.23	79.42
4	15	0.75	300	62.97	60.27
5	90	1.0	300	90.83	89.71
6	120	2.5	400	98.76	97.58
7	60	1.5	400	85.38	85.56
8	120	2.5	400	98.76	97.58
9	60	1.5	150	97.04	96.13
10	120	2.5	100	99.89	100.00
11	120	0.75	400	82.88	83.66
12	15	0.75	100	69.61	73.43
13	60	2.5	200	98.24	98.58
14	90	2.0	300	96.55	98.64
15	90	0.75	100	98.13	96.32
16	30	2.0	300	83.33	85.17
17	60	1.5	400	85.38	85.56
18	15	2.5	400	79.23	79.42
19	120	1.5	200	98.88	99.00
20	120	2.5	100	99.89	100.00

The equation expressed in terms of actual factors enables prediction of the reaction at specified levels of each factor. For each factor, the levels should be indicated in their original units. This equation should not be utilized to calculate the relative impact of each element because the coefficients have been scaled to account for the units of each factor and the intercept is not in the design space's center.

A correlation between predicted and actual adsorption (%) of AO7 dye on activated carbon is shown in Figure 14. It is clear from the figure that there is good agreement between the experimental values and the predicted model, which is validated by the high value of the correlation coefficient (R^2 = 0.9785). The ANOVA is given in Table 7 and is used to predict the cubic, individual, and interaction effects of the independent

variables on the adsorption of AO7 dye on activated carbon. The results suggest that the quadratic model (p-value < 0.05) has a significant contribution. The determination coefficient described the standard of the polynomial model as a basis of the extent of deviation through the mean elucidated by the model, and the values of Adj-R^2 = and R^2 = show a good correlation between the predicted and exponential data [78–81]. The Predicted R^2 of 0.7850 is in reasonable agreement with the Adjusted R^2 of 0.9591; i.e., the difference is less than 0.2. Adeq Precision measures the signal to noise (S/N) ratio. A ratio greater than 4 is desirable. The S/N value of 26.139 indicates an adequate signal, which shows a significant RSM-model signal that can be utilized for navigating the design [78,82].

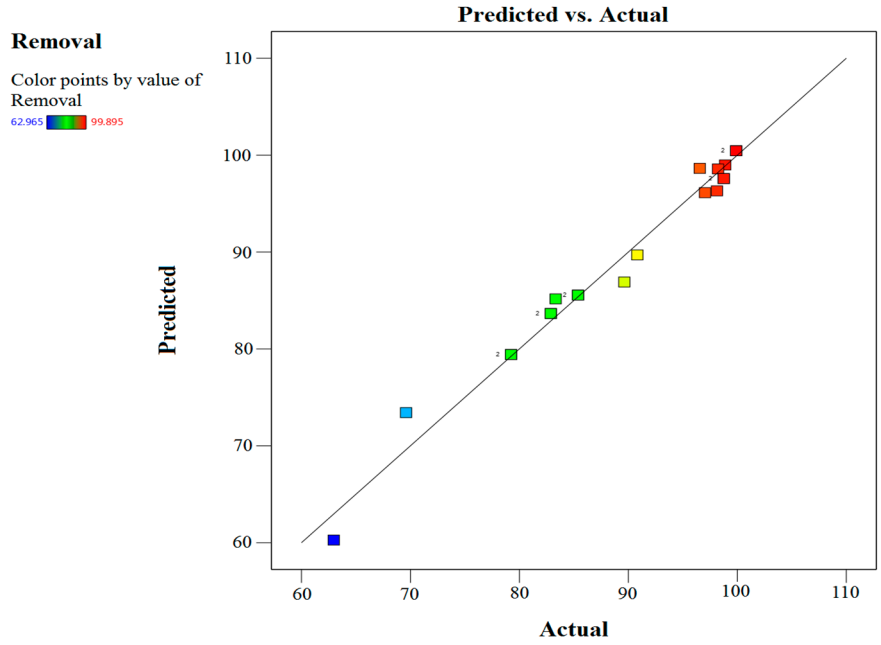

Figure 14. Plots between the predicted and experimental data for AO7 dye adsorption.

Table 7. ANOVA and model fit summary for D-optimal design.

Source	Value	Sum of Squares	df	Mean Square	F-Value	*p*-Value	Remarks	Source	SD	R^2	Adjusted R^2	Predicted R^2	PRESS	Remarks
Model	-	2150.07	9	238.90	50.54	<0.0001	significant	-	-	-	-	-	-	-
A-Time	-	1079.40	1	1079.40	228.34	<0.0001	-	-	-	-	-	-	-	-
B-Dose	-	513.89	1	513.89	108.71	<0.0001	-	-	-	-	-	-	-	-
C-Conc	-	351.46	1	351.46	74.35	<0.0001	-	-	-	-	-	-	-	-
AB	-	71.77	1	71.77	15.18	0.0030	-	-	-	-	-	-	-	-
AC	-	19.25	1	19.25	4.07	0.0712	-	-	-	-	-	-	-	-
BC	-	57.94	1	57.94	12.26	0.0057	-	-	-	-	-	-	-	-
A^2	-	121.18	1	121.18	25.64	0.0005	-	-	-	-	-	-	-	-
B^2	-	26.06	1	26.06	5.51	0.0408	-	-	-	-	-	-	-	-
C^2	-	0.0370	1	0.0370	0.0078	0.9312	-	-	-	-	-	-	-	-
Residual	-	47.27	10	4.73		-	-	-	-	-	-	-	-	-
Lack of Fit	-	47.27	5	9.45		-	-	-	-	-	-	-	-	-
Pure Error	-	0.0000	5	0.0000		-	-	-	-	-	-	-	-	-
Cor Total	-	2197.34	19	-	-	-	-	-	-	-	-	-	-	-
SD	2.17	-	-	-	-	-	-	-	-	-	-	-	-	-
Mean	8.88	-	-	-	-	-	-	-	-	-	-	-	-	-
C.V.%	2.45	-	-	-	-	-	-	-	-	-	-	-	-	-
R^2	0.9785	-	-	-	-	-	-	-	-	-	-	-	-	-
Adjusted R^2	0.9591	-	-	-	-	-	-	-	-	-	-	-	-	-
Predicted R^2	0.7850	-	-	-	-	-	-	-	-	-	-	-	-	-
Adeq Precision	26.1392	-	-	-	-	-	-	-	-	-	-	-	-	-
Linear									5.62	0.7699	0.7268	0.6104	856.03	
2FI									5.24	0.8377	0.7628	0.5614	963.71	
Quadratic									2.17	0.9785	0.9591	0.7850	472.47	Suggested
Cubic									0.0000	1.0000	1.0000	-	-	Aliased

Simultaneous Effects of Interactive Adsorption Variables

Three-dimensional surface plots present the effects and interactions of independent variables, namely contact time, activated carbon dose, and initial dye concentration, on the removal percentages of AO7 dye (Figure 15) as the responses.

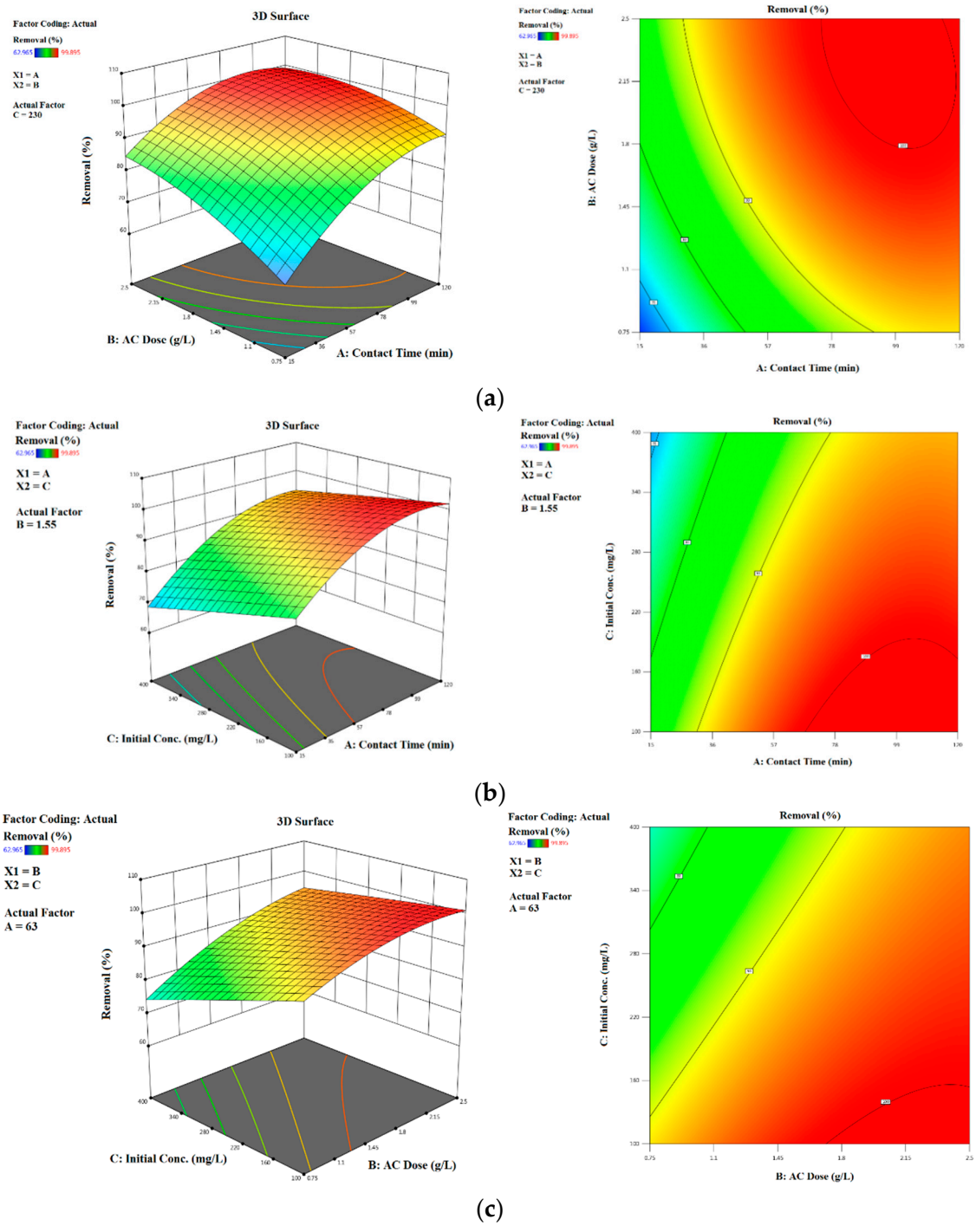

Figure 15. Combined effect of process variables: (**a**) adsorbent dosage and contact time, (**b**) initial concentra-tion and contact time, and (**c**) initial concentration and adsorbent dosage on AO7 dye removal with interaction effect of dual factor.

The interaction of initial ion concentration and adsorbent dosage shown in Figure 15c indicates the significant influence of both factors on the removal of AO7 dye. The removal percentages increased with increasing adsorbent dosage. This result was due to the presence

of additional active sites and a large adsorbent surface area that is readily available for adsorption [83,84]. The removal percentage was reduced by increasing the initial ion concentration, as shown in Figure 15b. This finding might be due to the limited active sites on the adsorbent surface at high AO7 dye concentrations [85]. The removal percentage was increased by increasing the residence time from 40 min to 60 min. These results confirmed that the initial adsorption rate was very rapid due to the availability of a large surface area and the presence of unused sites on the activated carbon surface [86]. The slowing down of dye removal might be due to the difficulty of reaching the re-maining vacant sites. To optimize and validate the predicted mathematical model, a complementary statistical design calculation was performed under the same experi-mental conditions; Figure 16 shows that the higher desirability value obtained from the results of the mathematical model is equal to 0.982. Using these conditions, the maximum removal (%) (Removal (%) = 99.895%, experimental) obtained corresponds to the contact time: 95.7 min, AC dose 2 g/L and initial AO7 dye concentration of 100 mg/L.

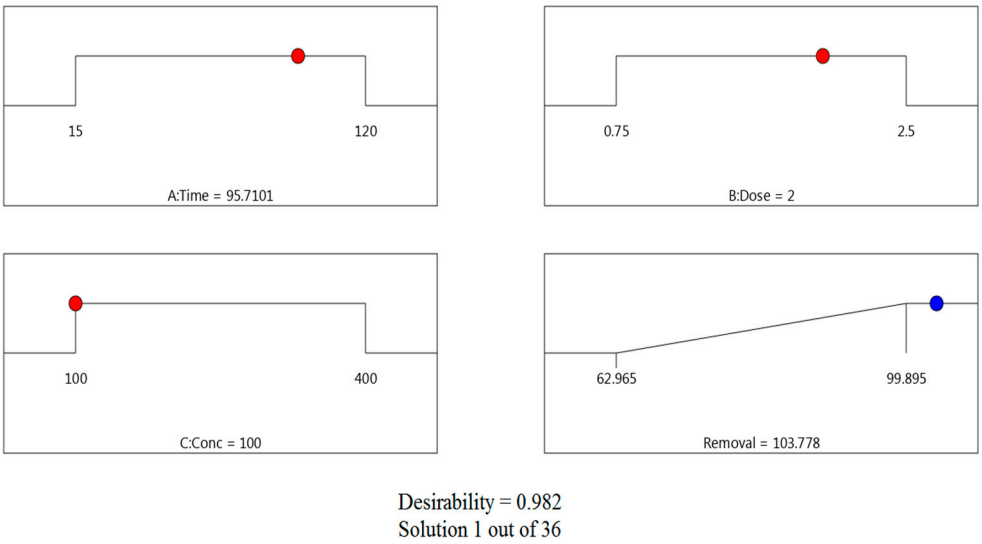

Figure 16. Optimum conditions predicted by RSM method.

3. Materials and Methods

3.1. Chemicals and Reagents

The raw material (*Pisum sativum* pea pods) employed in the present investigation as the raw material for the synthesis of activated carbon was obtained from a local market. After being scrubbed with tap water and distilled water to remove dirt and dust, these pea pods were sun-dried for two weeks before being used. Subsequently, the pea pods were powdered using a rotary mill at high speed and sieved through size <200 meshes. The powdered pea pods were kept in a cool, dry place until they were needed again. Potassium hydroxide (KOH) and zinc chloride ($ZnCl_2$) were purchased from El-Nasr Company, Egypt. The hydrochloric acid (HCl) used in this experiment was obtained from Sigma-Aldrich in the United States. It was unnecessary to purify the Acid Orange 7 (AO 7) dye (C.I. 15510; chemical formula, $C_{16}H_{11}N_2NaO_4S$; molecular weight 350.33 g mol^{-1}), which was obtained from Sigma-Aldrich in the United States. A stock solution of AO7 dye (1000 mg L^{-1}) was prepared by dissolving the required amount of AO7 dye in distilled water and allowing the solution to stand for 24 h. The stock solution was diluted with distilled water to the desired concentrations to make all of the relevant working solution concentrations. All chemicals utilized were of analytic grade and had not undergone any further purification before being used in this study.

3.2. Preparation of Activated Carbon

3.2.1. Impregnation with $ZnCl_2$

Sieved pea pod powder was soaked in distilled water, impregnated with $ZnCl_2$ in a 2:1 ratio (pea pods to $ZnCl_2$, weight-to-weight), then baked until dry at 105 °C. Successively dried impregnated mixture was placed in an alumina boat, loaded in a horizontal tube furnace, heated at a ramp rate of 10 °C min^{-1}, and kept at 600, 700, and 800 °C each for 60 min under a N_2 atmosphere; the entire pyrolysis process was repeated under a CO_2 atmosphere, for which the gas flow rate was 5 L min^{-1}. Then, the furnace temperature was cooled to room temperature, and the carbonized sample was removed from the furnace and boiled in 2 N HCl for 2 h to remove residual organic and mineral matters. The filtrate was then rinsed many times with warm distilled water to bring the pH back to a neutral range before being dried in an oven at 105 °C for 24 h to remove any remaining contaminants. Activated carbon samples were milled and sieved using a mesh size <60 μm to obtain homogenous particle size.

3.2.2. Impregnation with KOH

The sieved pea pod powder was impregnated with 10% KOH in distilled water. The impregnated mixture was dried at 105 °C in an oven for 24 h. Dried impregnated mixture was subjected to carbonization in an alumina boat in a horizontal tube furnace heated at a ramp rate of 10 °C min^{-1} and kept at 600, 700, and 800 °C each for 60 min under a N_2 atmosphere; the pyrolysis process was repeated under a CO_2 atmosphere. The carbon samples were cooled in a nitrogen or carbon dioxide environment, then removed from the furnace and repeatedly washed with distilled water until the filtrate's pH was neutral. A 2 h reflux in 2N HCl was used to remove organic and mineral debris from the carbon, followed by filtration and washing with deionized water to bring it to a pH neutral value of around 7. 24 h. Oven drying at 105 °C produced the desired activated carbon. Activated carbon samples were milled and sieved using a mesh size <60 μm to obtain homogenous particle size.

3.3. Characterization of the Synthesized Activated Carbons

Brunauer–Emmett–Teller (BET), t-Plot, MP, and BJH methods were used for the determination of specific surface area (S_{BET}), total pore volume, and mean pore size. They were estimated by the volume of nitrogen gas adsorbed to the activated carbon surface per unit mass of the measured samples using BELSORP Mini-II equipment, BEL Japan with a N_2 adsorption at 77 K as adsorption temperature and saturated vapor pressure of 89.62 kPa. The samples were pretreated at 300 °C under flow of nitrogen gas. The micropore volume and total pore volume were determined using the *t*-plot method. The volume of the mesopores (V_{MesoP}) was calculated using the difference between total pore volume (V_{TP}) and total micropore volume (V_{mP}). The average pore diameter (APD) was calculated using the $4V_{TP}/S_{BET}$ ratio. The functional groups on the activated carbon surface were examined by Fourier transform infrared spectroscopy (FTIR) analysis that was performed on the activated carbon using a Bruker Model Vertex 70 FTIR spectrometer coupled to a Platinum ATR unit using a spectral range of 4000–400 cm^{-1}, Bruker, Germany. Thermal analyses were performed using a SDT 650 TA Instrument—Waters LLC. The range was from 50 to 900 °C under a N_2 flow of 100 mL min^{-1}. The porosity and the surface morphology of the activated carbons obtained in this study were examined by SEM analysis performed using an FEI Quanta 250 FEG Scanning Electron Microscope using 500 KV HV, 2500–6000× magnification and large-field low vacuum SED (LED). XRD analysis was performed using a D2 PHASER Instrument, Bruker, Germany.

3.4. Adsorption Experiments

The prepared activated carbons were tested for AO7 dye removal, and the highest surface area activated carbon was selected for further evaluation of its AO7 dye removal through batch equilibrium adsorption studies depending on adsorption capacity. Batch

adsorption studies were performed using different initial concentrations of AO7 dye prepared by dilution of the feed stock solution of 1000 ppm with distilled water. All adsorption tests were performed in a shaking instrument at ambient temperatures. The pH values (1.5, 3.0, 4.1, 5.1, 7, 9, and 10) of solutions were adjusted before and during the experimental process using 0.1 M HCl or NaOH solutions. The different specified initial solution concentrations were introduced into flasks containing a known amount of the activated carbon at room temperature (24 ± 2 °C). The following parameters were investigated to understand their effects on AO7 dye adsorption onto the activated carbon surface: contact time from 0 to 180 min; pH from 1.5 to 10; adsorbent dosage of 0.75, 1.0, 1.5, 2.0, and 2.5 g L^{-1}; and feed solution initial concentration of 100, 150, 200, 300, and 400 mg L^{-1}. The initial and equilibrium concentrations were measured utilizing a UV–Vis spectrophotometer at a wavelength of λ_{max} 483 nm for AO7 dye using a double-beam spectrophotometer (SPEKOL 1300-ANALYTIK JENA AG-Germany). The suspension was shaken at 200 rpm and at predetermined time intervals. An amount of 1 mL of the clear solution was taken and analyzed using a UV–Vis spectrophotometer. Reported values are averages of the triplicated experiment. AO7 dye removal percentage (%R) was estimated according to the following Equation (4):

$$\%R = \frac{C_i - C_e}{C_i} \times 100 \quad (4)$$

where C_i and C_e are the AO7 dye concentrations (mg L^{-1}) pertaining to initial and equilibrium states of adsorption. Adsorption capacity of AO7 dye after time t (min) of adsorption on the activated carbon (Q_t) was calculated using the following Equation (5):

$$Q_t = \frac{(C_i - C_t)}{W} \times V \quad (5)$$

where C_t (mg L^{-1}), V (L), and W (g) are concentration of AO7 dye after time t, volume of initial feed solution taken, and the weight of activated carbon used as adsorbent, respectively. The equilibrium adsorption capacity Q_e (mg g^{-1}) for the prepared activated carbon was calculated with the following Equation (6):

$$Q_e = \frac{(C_0 - C_e) \times V}{W} \quad (6)$$

where the initial dye concentration is C_0 (mg L^{-1}) and the dye's equilibrium concentration is C_e (mg L^{-1}). V (L) is the dye solution's volume, while W (g) is the adsorbent's weight. The adsorption kinetic experiments were carried out in the same system with different concentrations of AO7 dye solution (100, 150, 200, 300, and 400 mg L^{-1}) using different concentrations of activated carbon (0.75, 1.0, 1.5, 2.0, and 2.5 g L^{-1}). In a certain time interval, the remaining concentrations of the AO7 dye were measured with a UV–Vis spectrophotometer.

3.5. Isotherm Models Study

Experimental equilibrium values were studied using five isotherm models: Langmuir [87], Freundlich [88], Tempkin [89], Harkins–Jura [90] and Halsey [91]. The best-fitting model was discovered through the use of linear regression. Adsorption occurs uniformly on the active sites of the adsorbent surface, according to Langmuir theory, and there are no molecular interactions between the adsorbate and the adsorbent, which results in the presence of a single-layer deposition on the surface of the adsorbent, which has identical active sites and has the maximum adsorption capacity (Q_m). As soon as the adsorbate occupies an active site, no further adsorption can take place at that site, and there is no further transmigration of the adsorbate in a plane parallel to the surface's surface tension [69]. The Langmuir isotherm model can be represented in linear relationships as in Equation (7) :

$$\frac{C_e}{Q_e} = \frac{1}{Q_m \times K_L} + \frac{C_e}{Q_m} \quad (7)$$

where Q_e is the equilibrium adsorption capacity of adsorbent (mg g^{-1}), Q_m is the maximum adsorption capacity (mg g^{-1}), and K_L is related to the Langmuir adsorption energy constant (L g^{-1}).

The Freundlich isotherm model [88] assumes the presence of interactions between adsorbed molecules which lead to the formation of multilayer adsorption on the adsorbent surface. Given that Freundlich's assertion is a linear equation, it implies that when the adsorbate concentration increases, the adsorbate concentration on the adsorbent surface increases as well. It is possible to present Freundlich's isotherm in linear form using Equation (8):

$$\ln(Q_e) = \ln(K_F) + \frac{1}{n} \times ln(C_e) \quad (8)$$

where K_F and n represent Freundlich isotherm constants corresponding to adsorption capacity and heterogeneity factor, respectively. A value for $1/n$ below one indicates a normal Langmuir isotherm, while $1/n$ above one is indicative of cooperative adsorption.

According to the Tempkin isotherm model [89], indirect interactions between adsorbate and adsorbate are theorized. This hypothesis stated that, as a result of adsorbent–adsorbate interactions, the heat of adsorption of all molecules in the layer decreases linearly with coverage and that adsorption is characterized by an even distribution of binding energies up to and including a maximum binding energy. Equation (9) explains the linear relation using the Tempkin isotherm model:

$$Q_e = \frac{RT}{b} \ln(K_T) + \frac{RT}{b} ln(C_e) \quad (9)$$

where K_T (L g^{-1}) is the Tempkin isotherm constant, b (J mol^{-1}) is the adsorption energy (heat of adsorption) variation factor, R (8.314 J mol^{-1} K^{-1}) is the universal gas constant, and T is the absolute temperature in Kelvin. Plotting Q_e versus ln C_e enables determination of isotherm constants B (RT/b) and K_T from slopes and intercepts, respectively. K_T (L/g) is the equilibrium-binding constant corresponding to the maximum binding energy, and constant B is related to the heat of the adsorption.

The Harkins–Jura isotherm model [90] takes into account multilayer adsorption as well as the adsorbent's heterogeneous pore distribution. The Harkins–Jura isotherm is frequently used in the form Equation (10):

$$\frac{1}{Q_e^2} = \left(\frac{B_{HJ}}{A_{HJ}}\right) - \left(\frac{1}{A_{HJ}}\right) log(C_e) \quad (10)$$

where A_{HJ} and B_{HJ} are the isotherm constant and multilayer adsorption heterogeneous pore distribution. The Halsey isotherm model [91] is applicable to multilayer adsorption, and heteroporous substances can be used to fit the Halsey equation [91,92]. The Halsey model is frequently used with the following Equation (11):

$$\ln(Q_e) = \left[\left(\frac{1}{n_H}\right) ln(K_H)\right] + \left(\frac{1}{n_H}\right) ln(C_e) \quad (11)$$

where n_H and K_H are Halsey constants.

3.6. Adsorption Kinetic Models Study

To comprehend the adsorption kinetics pattern, the collected experimental data were fitted to the described kinetic models. Lagergren's pseudo-first-order Equation (12) [69,93] is as follows:

$$\log(Q_e - Q_t) = logQ_e - \frac{K_1}{2.303} t \quad (12)$$

K_1 (g mg^{-1} min^{-1}) is the first-order rate constant, and Q_t and Q_e (mg g^{-1}) are the adsorption capacities at time t (min) and equilibrium, respectively. Equation (13) can be used to express the pseudo-second-order model [69,94]:

$$\frac{t}{Q_t} = \frac{1}{K_2 Q_e^2} + \frac{t}{Q_e} \tag{13}$$

where K_2 is the second-order rate constant (g mg^{-1} min^{-1}). The intercept and slope of the plot generated by plotting t/Q_t versus t can be used to compute K_2 and Q_e [69]. The Elovich kinetic equation is another rate equation that is based on adsorption capacity and is typically represented as Equation (14) [69,95]:

$$\frac{dQ_t}{dt} = \alpha\, exp(-\beta Q_t) \tag{14}$$

where α is the initial adsorption rate (mg g^{-1} min^{-1}) and β is the desorption constant (g mg^{-1}) during the course of a single experiment. It is simplified by assuming $\alpha\beta t >> t$ and by applying the boundary conditions $Q_t = 0$ at $t = 0$, and $Q_t = Q_t$ at $t = t$ simplifies the following Equation (13) to form Equation (15):

$$Q_t = \frac{1}{\beta}\ln(\propto \beta) + \frac{1}{\beta} ln(t) \tag{15}$$

A plot of Q_t versus ln(t) should yield a linear relationship with a slope of (1/β) and an intercept of (1/β) × ln($\alpha\beta$). Thus, the constants may be determined from the straight line's slope and intercept. The experimental data were also fitted using the intraparticle diffusion model Equation (16) [69,96]:

$$Q_t = K_{dif} t^{0.5} + C \tag{16}$$

where K_{dif} (mg g^{-1} min$^{0.5}$) is the intraparticle diffusion rate constant and C (mg g^{-1}) is a constant revealing the thickness of the boundary layer. The liquid film diffusion model [69,97] can be used when the transfer of solute molecules from the liquid phase to the solid phase boundary plays a major role in adsorption (Equation (17)):

$$\ln(1 - F) = K_{FD}(t) \tag{17}$$

where K_{FD} *and* F ($F = Q_t/Q_e$) are the film diffusion rate constant and the fractional attainment of equilibrium, respectively.

3.7. Optimization Study Response Surface Methodology (RSM)

In contrast to the other forms of RSM designs, such as central composite or Box–Behnken, the historical data design and optimal custom design of RSM enable the construction of mathematical models based on previously collected experimental data [98]. The D-optimal design was studied using the Stat-Ease Design-Expert v13.0.5.0 program to investigate the adsorption of AO7 dye from the adsorbent coating. Using response surface methods (RSM), the impacts of three independent variables (A: contact time, B: activated carbon dose, and C: beginning AO7 dye concentration) on the response (R: dye removal %) were investigated. RSM is a statistical technique that utilizes quantitative data from appropriate experiments to establish the regression model equations and operating parameters. The optimization procedure consists of three steps: executing a statistically planned experiment, determining mathematical model coefficients and response value prediction, and checking the produced model's suitability [83]. The experiment's range and variable are listed in Table 8.

Table 8. Range and levels used for the batch adsorption study.

Independent Variables	Notation	Unit	Range and Levels of Actual and Coded Values				
			$-\alpha$	-1	0	1	α
Time	A X1	min	15	30	60	90	120
Dosage	B X2	g/L	0.75	1	1.5	2	2.5
Concentration	C X3	mg/L	100	150	200	300	400

Six axial points, eight factorial points, and six replicates at the central point were used to create the best bespoke design for the three independent variables. The factors chosen were varied on a five-level scale ($-\alpha$, -1, 0, 1, $+\alpha$). The number of experiment runs was calculated based on Equation (18):

$$N = 2^k + 2k + C = 2^3 + 2.3 + 6 \quad (18)$$

where N is the total number of runs, k denotes the total number of factors to be tested, and C denotes the total number of experiments completed at the center. Table 8 shows the lower and upper bounds for each factor. State-Ease Design-Expert v 13.0.5.0 was used to generate the experiment data matrix. Study of variance was used to conduct a statistical analysis of the generated model (ANOVA). Surface contour plots were used to investigate the relationships between factors.

4. Conclusions

The synthesis of activated carbon from *Pisum sativum* pea pods was demonstrated in this work employing a 2:1 ratio of $ZnCl_2$ and a 10 percent solution of KOH as activation reagents. The impregnated biomass was activated at different temperatures (600, 700, and 800 °C) under N_2 and CO_2 gases for 60 min. It is worth noting that the chemical activation reagents and the gas medium to be treated had a significant effect on the surface area and pore structure of activated carbons, with $ZnCl_2$ and CO_2 being preferred. To optimize the activation settings, the response surface methodology was successfully employed. The optimal conditions for the removal of AO7 dye were determined to be carbon impregnated with a 2:1 ratio of $ZnCl_2$ under CO_2 gas at 800 °C and AO7 dye solution at pH 1.5, which achieved a removal percentage of 100%. Using SEM images, it was discovered that a pore structure had formed in the AC-$ZnCl_2$ during the activation phase. The AC-$ZnCl_2$ under CO_2 at 800 °C exhibited a high surface area (S_{BET}) of 1300 to 1500 $m^2\ g^{-1}$, a total pore volume of 0.6176 $cm^3\ g^{-1}$, and a mean pore diameter of 1.901 nm. Based on the experimental maximum adsorption capacity at equilibrium was 467.16 mg g^{-1} and the maximum percentages removal of AO7 dye was ~100%. It is possible to conclude that the adsorption mechanism of AO7 dye onto AC-$ZnCl_2$ is a process of monolayer formation and governed by physisorption, which is best modelled with the Langmuir isotherm and obeys the pseudo-second-order and film diffusion kinetic models. The maximum adsorption capacity (Q_m) for AO7 dye determined in this work using a selective activation approach was 473.93 mg g^{-1}, which is significantly higher than the adsorption capacity of numerous activated carbons previously reported in the literature. As a result, it has the potential to be employed as a viable adsorbent biomaterial for the removal of AO7 dye from aqueous solutions.

Supplementary Materials: The following are available online at https://www.mdpi.com/article/10.3390/molecules27154840/s1, **Figure S1**. BET analysis of AC prepared from pea pods impregnated with using (a) KOH and carbonized under N_2 gas flow, (b) KOH and carbonized under CO_2 gas flow, (c) $ZnCl_2$ and carbonized under N_2 gas flow, and (d) $ZnCl_2$ and carbonized under CO_2 gas flow. **Figure S2**. The t-plot analysis of AC prepared from pea pods impregnated with using (a) KOH and carbonized under N_2 gas flow, (b) KOH and carbonized under CO_2 gas flow, (c) $ZnCl_2$ and carbonized under N_2 gas flow, and (d) $ZnCl_2$ and carbonized under CO_2 gas flow. **Figure S3**. (a) MP analysis of AC KOH-N_2 (b) MP analysis of AC KOH-CO_2, (c) MP analysis of AC $ZnCl_2$-N_2 (d) MP analysis of AC $ZnCl_2$-CO_2.

Author Contributions: M.A.E.-N.; conceived the main idea of the paper, performed the experiment and theoretical calculation. A.E.N.; designed the experiment, supervised the work, and revised the manuscript. S.R.; wrote the original manuscript. M.A.H.; helped in preparing the manuscript. A.P., L.T., and G.D.M. contributed various comments and ideas to help improve the overall quality of the research. All authors have read and agreed to the published version of the manuscript.

Funding: This research received no external funding.

Institutional Review Board Statement: Not applicable.

Informed Consent Statement: Not applicable.

Data Availability Statement: The data presented in this study are available in the manuscript and Supplementary Material.

Conflicts of Interest: The authors declare no conflict of interest.

References

1. Yuan, X.Z.; Choi, S.W.; Jang, E.; Lee, K.B. Chemically activated microporous carbons derived from petroleum coke: Performance evaluation for CF4 adsorption. *Chem. Eng. J.* **2018**, *336*, 297–305. [CrossRef]
2. Du, Y.; Xu, X.; Liu, Q.; Bai, L.; Hang, K.; Wang, D. Identification of organic pollutants with potential ecological and health risks in aquatic environments: Progress and challenges. *Sci. Total. Environ.* **2021**, *806*, 50691. [CrossRef] [PubMed]
3. Pavithra, K.G.; Jaikumar, V.; Kumar, P.S.; Sundarrajan, P. Removal of emerging pollutants from aquatic system using electrochemical treatment and adsorption: Comparison and analysis. *Environ. Technol. Innov.* **2021**, *23*, 101754. [CrossRef]
4. El Nemr, A. *Impact, Monitoring and Management of Environmental Pollution*; Nova Science Publishers/Inc. Hauppauge: New York, NY, USA, 2021; p. 638, ISBN-10: 1608764877, ISBN-13: 9781608764877.
5. Hassaan, M.A.; El Nemr, A.; Madkour, F.F. Testing the advanced oxidation processes on the degradation of Direct Blue 86 dye in wastewater. *Egypt. J. Aquat. Res.* **2017**, *43*, 11–19. [CrossRef]
6. Luo, P.; Zhao, Y.F.; Zhang, B.; Liu, J.D.; Yang, Y.; Liu, J.F. Study on the adsorption of Neutral Red from aqueous solution onto halloysite nanotubes. *Water Res.* **2010**, *44*, 1489–1497. [CrossRef]
7. Acemioğlu, B. Adsorption of congo red from aqueous solution onto calcium-rich fly ash. *J. Colloid Interface Sci.* **2004**, *274*, 371–379. [CrossRef] [PubMed]
8. Sahlabji, T.; El-Nemr, M.A.; El Nemr, A.; Ragab, S.; Alghamdi, M.M.; El-Zahhar, A.A.; Idris, A.M.; Said, T.O. High Surface Area Microporous Activated Carbon from *Pisum sativum* peels for Hexavalent Chromium Removal from Aquatic Environment. *Toxin Rev.* **2022**, *41*, 639–649. [CrossRef]
9. Ajmal, A.; Majeed, I.; Malik, R.N.; Idriss, H.; Nadeem, M.A. Principles and mechanisms of photocatalytic dye degradation on TiO_2 based photocatalysts: A comparative overview. *RSC Adv.* **2014**, *4*, 37003–37026. [CrossRef]
10. Helmy, E.T.; El Nemr, A.; Gomaa, E.; El Dafrawy, S.; Mousa, M. Photocatalytic degradation of textile dyeing wastewater under visible light irradiation using green synthesized mesoporous non-metal doped TiO_2. *Bull. Mater. Sci.* **2021**, *44*, 30. [CrossRef]
11. Güzel, F.; Shaygılı, H.; Saygılı, G.A.; Koyuncu, F. New low-cost nanoporous carbonaceous adsorbent developed from carob (Ceratonia siliqua) processing industry waste for the adsorption of anionic textile dye: Characterization, equilibrium and kinetic modeling. *J. Mol. Liq.* **2015**, *206*, 244–255. [CrossRef]
12. El-Nemr, M.A.; Abdelmonem, N.M.; Ismail, I.M.A.; Ragab, S.; El Nemr, A. Removal of Acid Yellow 11 Dye using novel modified biochar derived from Watermelon Peels. Desal. *Desal. Water Treat.* **2020**, *203*, 403–431. [CrossRef]
13. El-Nemr, M.A.; Abdelmonem, N.M.; Ismail, I.M.A.; Ragab, S.; El Nemr, A. The efficient removal of the hazardous Azo Dye Acid Orange 7 from water using modified biochar from Pea peels. Desal. *Desal. Water Treat.* **2020**, *203*, 327–355. [CrossRef]
14. El Nemr, A. *Textiles: Types, Uses and Production Methods*; Nova Science Publishers/Inc. Hauppauge: New York, NY, USA, 2012; p. 621, ISBN: 978-1-62100-239-0, ISBN: 978-1-62100-284-0.
15. Mahmoodi, N.M.; Taghizadeh, M.; Mesoporous, A.T. Mesoporous activated carbons of low-cost agricultural bio-wastes with high adsorption capacity: Preparation and artificial neural network modeling of dye removal from single and multicomponent (binary and ternary) systems. *J. Mol. Liq.* **2018**, *269*, 217–228. [CrossRef]
16. Hassaan, M.A.; El Nemr, A.; El-Zahhar, A.A.; Idris, A.M.; Alghamdi, M.M.; Sahlabji, T.; Said, T.O. Degradation mechanism of Direct Red 23 dye by advanced oxidation processes: A comparative study. *Toxin Rev.* **2022**, *41*, 38–47. [CrossRef]
17. El Nemr, A. *Non-Conventional Textile Waste Water Treatment*; Nova Science Publishers, Inc. Hauppauge: New York, NY, USA, 2012; p. 267, ISBN: 978-1-62100-079-2, ISBN: 978-1-62100-228-4.
18. Hosseini, S.A.; Vossoughi, M.; Mahmoodi, N.M.; Sadrzadeh, M. Efficient dye removal from aqueous solution by high-performance electrospun nanofibrous membranes through incorporation of SiO_2 nanoparticles. *J. Clean. Prod.* **2018**, *183*, 1197–1206. [CrossRef]
19. El Nemr, A.; Shoaib, A.G.M.; El Sikaily, A.; Ragab, S.; Mohamed, A.E.-D.A.; Hassan, A.F. Utilization of green alga *Ulva lactuca* for sustainable production of meso-micro porous nano activated carbon for adsorption of Direct Red 23 dye from aquatic environment. *Carbon Lett.* **2022**, *32*, 153–168. [CrossRef]

20. El Nemr, A.; Aboughaly, R.M.; El Sikaily, A.; Ragab, S.; Masoud, M.S.; Ramadan, M.S. Utilization of *Citrus aurantium* peels for sustainable production of high surface area type I microporous nano activated carbons. *Biomass Convers. Biorefin.* **2021**. [CrossRef]
21. El Nemr, A.; Aboughaly, R.M.; El Sikaily, A.; Masoud, M.S.; Ramadan, M.S.; Ragab, S. Microporous activated carbons with a high surface area of type I adsorption isotherm derived from sugarcane bagasse impregnated with zinc chloride. *Carbon Letter.* **2022**, *32*, 229–249. [CrossRef]
22. Shoaib, A.G.M.; El-Sikaily, A.; El Nemr, A.; Mohamed, A.E.-D.A.; Hassan, A.A. Testing the carbonization condition for high surface area preparation of activated carbon followed Type IV from green alga *Ulva lactuca*. *Biomass Convers. Biorefin.* **2020**, *12*, 3303–3318 . [CrossRef]
23. Shoaib, A.G.M.; El-Sikaily, A.; El Nemr, A.; Mohamed, A.E.-D.A.; Hassan, A.A. Preparation and characterization of highly surface area activated carbons followed Type IV from marine red alga (*Pterocladia capillacea*) by zinc chloride activation. *Biomass Convers. Biorefin.* **2022**, *12*, 2253–2265. [CrossRef]
24. El Nemr, A.; Aboughaly, R.M.; El Sikaily, A.; Ragab, S.; Masoud, M.S.; Ramadan, M.S. Microporous nano activated carbon type I derived from orange peel and its application for Cr(VI) removal from aquatic environment. *Biomass Convers. Biorefin.* 2020, *in press*. [CrossRef]
25. Carrott, P.J.M.; Suhas, R.; Carrott, M.M.L.; Guerrero, C.I.; Delgado, L.A. Reactivity and porosity development during pyrolysis and physical activation in CO_2 or steam of kraft and hydrolytic lignins. *J. Anal. Appl. Pyrol.* **2008**, *82*, 264–271. [CrossRef]
26. Liu, Q.S.; Zheng, T.; Wang, P.; Guo, L. Preparation and characterization of activated carbon from bamboo by microwave-induced phosphoric acid activation. *Ind. Crops Prod.* **2010**, *31*, 233–238. [CrossRef]
27. Álvarez, P.; Blanco, C.; Granda, M. The adsorption of chromium (VI) from industrial wastewater by acid and base activated lignocellulosic residues. *J. Hazard. Mater.* **2007**, *144*, 400–405. [CrossRef] [PubMed]
28. El Nemr, A. Potential of pomegranate husk carbon for Cr(VI) removal from wastewater: Kinetic and isotherm studies. *J. Hazard. Mater.* **2009**, *161*, 132–141. [CrossRef]
29. Guo, J.; Lua, A.C. Textural and chemical characterisations of activated carbon prepared from oil-palm stone with H_2SO_4 and KOH impregnation. *Microporous Mesoporous Mater.* **2007**, *32*, 111–117. [CrossRef]
30. Carvalho, A.P.; Gomes, M.; Mestre, A.S.; Pires, J.; de Carvalho, M.B. Activated carbons from cork waste by chemical activation with K_2CO_3. Application to adsorption of natural gas components. *Carbon* **2004**, *42*, 672–674. [CrossRef]
31. Hayashi, J.; Kazehaya, A.; Muroyama, K.; Watkinson, A.P. Preparation of activated carbon from lignin by chemical activation. *Carbon* **2000**, *38*, 1873–1878. [CrossRef]
32. Dias, J.M.; Alvim-Ferraz, M.C.; Almeida, M.F.; Rivera-Utrill, J.; Sánchez-Polo, M. Waste materials for activated carbon preparation and its use in aqueous phase treatment: A review. *J. Environ. Manag.* **2007**, *85*, 833–846. [CrossRef]
33. Ogungbenro, A.E.; Quang, D.V.; Al-Ali, K.; Abu-Zahra, M.R. Activated carbon from date seeds for CO_2 capture application. *Energ. Procedia* **2017**, *114*, 2313–2321. [CrossRef]
34. Tan, X.; Liu, S.; Liu, Y.; Gu, Y.; Zeng, G.; Hu, X. Biochar as potential sustainable precursors for activated carbon production: Multiple applications in environmental protection and energy storage. *Bioresour. Technol.* **2017**, *227*, 359–372. [CrossRef] [PubMed]
35. Kadirvelu, K.; Kavipriya, M.; Karthika, C.; Radhika, M.; Vennilamani, N.; Pattabhi, S. Utilization of various agricultural wastes for activated carbon preparation and application for the removal of dyes and metal ions from aqueous solutions. *Bioresour. Technol.* **2003**, *87*, 129–132. [CrossRef]
36. Hameed, B.H.; Ahmad, A.L.; Latiff, K.N.A. Adsorption of basic dye (methylene blue) onto activated carbon prepared from rattan sawdust. *Dye. Pigment.* **2007**, *75*, 143–149. [CrossRef]
37. Kumar, B.G.P.; Miranda, L.R.; Velan, M. Adsorption of bismark brown dye on activated carbons prepared from rubberwood sawdust (Hevea brasiliensis) using different activation methods. *J. Hazard. Mater.* **2005**, *126*, 63–70. [CrossRef]
38. Garg, V.K.; Amita, M.; Kumar, R.; Gupta, R. Basic dye (methylene blue) removal from simulated wastewater by adsorption using Indian Rosewood sawdust: A timber industry waste. *Dyes Pigment.* **2004**, *63*, 243–250. [CrossRef]
39. Senthilkumaar, S.; Varadarajan, P.R.; Porkodi, K.; Subbhuraam, C.V. Adsorption of methylene blue onto jute Fiber carbon: Kinetics and equilibrium studies. *J. Coll. Interface Sci.* **2005**, *284*, 78–82. [CrossRef]
40. Attia, A.A.; Girgis, B.S.; Khedr, S. Capacity of activated carbon derived from pistachio shells by H_3PO_4 in the removal of dyes and phenolics. *J. Chem. Technol. Biotechnol.* **2003**, *78*, 611–619. [CrossRef]
41. Aygün, A.; Yenisoy-Karakaş, S.; Duman, I. Production of granular activated carbon from fruit stones and nutshells and evaluation of their physical, chemical and adsorption properties. *Micropor. Mesopor. Mater.* **2003**, *66*, 189–195. [CrossRef]
42. Kannan, N.; Meenakshisundaram, M. Adsorption of Congo Red on various activated carbons. *Water Air Soil Poll.* **2002**, *138*, 289–305. [CrossRef]
43. Tan, I.A.W.; Hameed, B.H.; Ahmad, W.A.L. Equilibrium and kinetic studies on basic dye adsorption by oil palm Fiber activated carbon. *Chem. Eng. J.* **2007**, *127*, 111–119. [CrossRef]
44. Krishnamoorthy, R.; Govindan, B.; Banat, F.; Sagadevan, V.; Purushothaman, M.; Show, P.L. Date pits activated carbon for divalent lead ions removal. *J. Biosci. Bioeng.* **2019**, *128*, 88–97. [CrossRef] [PubMed]
45. Sankar, M.; Sekaran, G.; Sadulla, S.; Ramasami, T. Removal of diazo and triphenylmethane dyes from aqueous solutions through an adsorption process. *J. Chem. Technol. Biotechnol.* **1999**, *74*, 337–344. [CrossRef]
46. Kavitha, D.; Namasivayam, C. Experimental and kinetic studies on methylene blue adsorption by coir pith carbon. *Bioresour. Technol.* **2007**, *98*, 14–21. [CrossRef]

47. Vasanth, K.; Kumaran, A. Removal of methylene blue by mango seed kernel powder. *Biochem. Eng. J.* **2005**, *27*, 83–93.
48. Kannan, N.; Sundaram, M.M. Kinetics and mechanism of removal of methylene blue by adsorption on various carbons—A comparative study. *Dyes Pigment.* **2001**, *51*, 25–40. [CrossRef]
49. Macedo, J.S.; Júnior, N.B.; Almeida, L.E. Kinetic and calorimetric study of the adsorption of dyes on mesoporous activated carbon prepared from coconut coir dust. *J. Coll. Interface Sci.* **2006**, *298*, 515–522. [CrossRef]
50. Geçgel, Ü.; Sezer, K.; Kolancılar, H. Removal of Cu(II) ions from aqueous solutions by the activated carbon obtained from pine cone. *Asian J. Chem.* **2010**, *22*, 3936–3942.
51. Gupta, V.K.; Jain, R.; Varshney, S. Removal of Reactofix golden yellow 3 RFN from aqueous solution using wheat husk—An agricultural waste. *J. Hazard. Mater.* **2007**, *142*, 443–448. [CrossRef]
52. Danish, M.; Ahmad, T.; Majeed, S.; Ahmad, M.; Ziyang, L.; Pin, Z.; Iqubal, S.M.S. Use of banana trunk waste as activated carbon in scavenging methylene blue dye: Kinetic, thermodynamic, and isotherm studies. *Bioresour. Technol. Rep.* **2018**, *3*, 127–137. [CrossRef]
53. Jung, K.W.; Choi, B.H.; Hwang, M.J.; Jeong, T.U.; Ahn, K.H. Fabrication of granular activated carbons derived from spent coffee grounds by entrapment in calcium alginate beads for adsorption of acid orange 7 and methylene blue. *Bioresour. Technol.* **2016**, *219*, 185–195. [CrossRef]
54. Ahmed, S.; Ahmed, A.; Rafat, M. Impact of aqueous and organic electrolytes on the supercapacitive performance of activated carbon derived from pea skin. *Surf. Coat. Technol.* **2018**, *349*, 242–250. [CrossRef]
55. Huang, Y.; Ma, E.; Zhao, G. Thermal and structure analysis on reaction mechanisms during the preparation of activated carbon fibers by KOH activation from liquefied wood-based fibers. *Ind. Crops Prod.* **2015**, *69*, 447–455. [CrossRef]
56. Heschel, W.; Klose, E. On the Suitability of Agricultural Byproducts for the Manufacture of Granular Activated Carbon. *Fuel* **1995**, *74*, 1786–1791. [CrossRef]
57. Hsu, L.-Y.; Teng, H. Influence of different chemical reagents on the preparation of activated carbons from bituminous coal. *Fuel Processing Technol.* **2000**, *64*, 55–166. [CrossRef]
58. Ahmadpour, A.; Do, D.D. The preparation of active carbons from coal by chemical and physical activation. *Carbon* **1996**, *34*, 471–479. [CrossRef]
59. Tseng, R.-L.; Tseng, S.-K.; Wu, F.-C.; Hu, C.-C.; Wang, C.-C. Effects of micropore development on the physicochemical properties of KOH-activated carbons. *J. Chin. Inst. Chem. Eng.* **2008**, *39*, 37–47. [CrossRef]
60. Muniandy, L.; Adam, F.; Mohamed, A.R.; Ng, E.-P. The synthesis and characterization of high purity mixed microporous/mesoporous activated carbon from rice husk using chemical activation with NaOH and KOH. *Micropor. Mesopor. Mater.* **2014**, *197*, 316–323. [CrossRef]
61. Mopoung, S.; Moonsri, P.; Palas, W.; Khumpai, S. Characterization and Properties of Activated Carbon Prepared from Tamarind Seeds by KOH Activation for Fe(III) Adsorption from Aqueous Solution. *Sci. World J.* **2015**, *9*, 415961. [CrossRef]
62. Gao, Y.; Yue, Q.; Gao, B.; Sun, Y.; Wang, W.; Li, Q. Preparation of high surface area-activated carbon from lignin of papermaking black liquor by KOH activation for Ni(II) adsorption. *Chem. Eng. J.* **2013**, *217*, 345–353. [CrossRef]
63. Guo, H.; Chen, Y.; Yang, S.; Li, R.; Zhang, X.; Dong, Q.; Li, X.; Ma, X. Lignin-based adsorbent-catalyst with high capacity and stability for polychlorinated aromatics removal. *Bioresour. Technol.* **2021**, *337*, 125453. [CrossRef]
64. Zhang, J.; Gao, J.; Chen, Y.; Hao, X.; Jin, X. Characterization, preparation, and reaction mechanism of hemp stem based activated carbon. *Results Phys.* **2017**, *7*, 1628–1633. [CrossRef]
65. Ragab, S.; El Nemr, A. Nanofiber Cellulose Di-and Tri-acetate Using Ferric Chloride as a Catalyst Promoting Highly Efficient Synthesis under Microwave irradiation. *J. Macromol. Sci. Part A Pure Appl. Chem.* **2018**, *55*, 124–134. [CrossRef]
66. Lozano-Castelló, D.; Calo, J.M.; Cazorla-Amorós, D.; Linares-Solano, A. Carbon activation with KOH as explored by temperature programmed techniques, and the effects of hydrogen. *Carbon* **2007**, *45*, 2529–2536. [CrossRef]
67. Lv, Y.; Gan, L.; Liu, M.; Xiong, W.; Xu, Z.; Zhu, D.; Wright, D.S. A self-template synthesis of hierarchical porous carbon foams based on banana peel for supercapacitor electrodes. *J. Power Sour.* **2012**, *209*, 152–157. [CrossRef]
68. El Nemr, A.; Ragab, S.; El Sikaily, A. Rapid synthesis of cellulose triacetate from cotton cellulose and its effect on specific surface area and particle size distribution. *Iran. Polym. J.* **2017**, *26*, 261–272. [CrossRef]
69. El Nemr, A.; El-Sikaily, A.; Khaled, A. Modeling of adsorption isotherms of Methylene Blue onto rice husk activated carbon. *Egypt. J. Aquat. Res.* **2010**, *36*, 403–425.
70. Anoopkrishnan, K.; Sreejalekshmi, K.G.; Baiju, R.S. Nickel(II) adsorption onto biomass based activated carbon obtained from sugarcane bagasse pith. *Bioresour. Technol.* **2011**, *102*, 10239–10247. [CrossRef]
71. Renugadevi, N.; Anitha, G.; Lalitha, P. Hexavalent chromium removal using a low-cost activated carbon adsorbent from Areca catechu. *Ind. J. Environ. Prot.* **2011**, *31*, 52–58.
72. Janos, P.; Buchtova, H.; Ryznarova, M. Sorption of Dyes from Aqueous Solutions onto Fly Ash. *Water Res.* **2003**, *37*, 4938–4944. [CrossRef]
73. Janos, P.; Coskun, S.; Pilarova, V.; Rejnek, J. Removal of Basic (Methylene Blue) and Acid (Egacid Orange) Dyes from Waters by Sorption on Chemically Treated Wood Shavings. *Bioresour. Technol.* **2009**, *100*, 1450–1453. [CrossRef]
74. Janos, P.; Sedivy, P.; Ryznarova, M.; Grotschelova, S. Sorption of Basic and Acid Dyes from Aqueous Solutions onto Oxihumolite. *Chemosphere* **2005**, *59*, 881–886. [CrossRef] [PubMed]

75. Li, J.; Du, Y.; Deng, B.; Zhu, K.; Zhang, H. Activated carbon adsorptive removal of azo dye and peroxydisulfate regeneration: From a batch study to continuous column operation. *Environ. Sci. Pollut. Res.* **2017**, *24*, 4932–4941. [CrossRef] [PubMed]
76. Gerçel, Ö.; Gerçel, H.F. Removal of Acid Dyes from Aqueous Solutions using Chemically Activated Carbon. *Sep. Sci. Technol.* **2009**, *44*, 2078–2095. [CrossRef]
77. Supriya, S.; Palanisamy, P.N. Adsorptive removal of acid orange 7 from industrial effluents using activated carbon and conducting polymer composite–A comparative study. *Ind. J. Chem. Technol.* **2016**, *23*, 506–512.
78. Sawood, G.M.; Mishra, A.; Gupta, S.K. Optimization of Arsenate Adsorption over Aluminum-Impregnated Tea Waste Biochar Using RSM–Central Composite Design and Adsorption Mechanism. *J. Hazard. Toxic Radioact. Waste* **2021**, *25*, 04020075. [CrossRef]
79. Schwaab, M.; Steffani, E.; Barbosa-Coutinho, E.; Júnior, J.B.S. Critical analysis of adsorption/diffusion modelling as a function of time square root. *Chem. Eng. Sci.* **2017**, *173*, 179–186. [CrossRef]
80. Lutzu, G.A.; Ciurli, A.; Chiellini, C.; Di Caprio, F.; Concas, A.; Dunford, N.T. Latest developments in wastewater treatment and biopolymer production by microalgae. *J. Environ. Chem. Eng.* **2021**, *9*, 104926. [CrossRef]
81. Dil, E.A.; Ghaedi, M.; Asfaram, A. Application of hydrophobic deep eutectic solvent as the carrier for ferrofluid: A novel strategy for pre-concentration and determination of mefenamic acid in human urine samples by high performance liquid chromatography under experimental design optimization. *Talanta* **2019**, *202*, 526–530. [CrossRef]
82. Bagheri, R.; Ghaedi, M.; Asfaram, A.; Dil, E.A.; Javadian, H. RSM-CCD design of malachite green adsorption onto activated carbon with multimodal pore size distribution prepared from Amygdalus scoparia: Kinetic and isotherm studies. *Polyhedron* **2019**, *171*, 464–472. [CrossRef]
83. Isam, M.; Baloo, L.; Kutty, S.R.M.; Yavari, S. Optimisation and modelling of Pb (II) and Cu (II) biosorption onto red algae (gracilaria changii) by using response surface methodology. *Water* **2019**, *11*, 2325. [CrossRef]
84. Mondal, N.K.; Samanta, A.; Roy, P.; Das, B. Optimization study of adsorption parameters for removal of Cr(VI) using Magnolia leaf biomass by response surface methodology. *Sustain. Water Resour. Manag.* **2019**, *5*, 1627–1639. [CrossRef]
85. Roy, P.; Dey, U.; Chattoraj, S.; Mukhopadhyay, D.; Mondal, N.K. Modeling of the adsorptive removal of arsenic (III) using plant biomass: A bioremedial approach. *Appl. Water Sci.* **2017**, *7*, 1307–1321. [CrossRef]
86. Lingamdinne, L.P.; Koduru, J.R.; Chang, Y.Y.; Karri, R.R. Process optimization and adsorption modeling of Pb(II) on nickel ferrite-reduced graphene oxide nano-composite. *J. Mol. Liq.* **2018**, *250*, 202–211. [CrossRef]
87. Langmuir, I. The constitution and fundamental properties of solids and liquids. *J. Am. Chem. Soc.* **1916**, *38*, 2221–2295. [CrossRef]
88. Freundlich, H.M.F. Über die adsorption in lösungen. *Z. Phys. Chem.* **1906**, *57A*, 385–470. [CrossRef]
89. Tempkin, M.J.; Pyzhev, V. Kinetics of Ammonia Synthesis on Promoted Iron Catalysts. *Acta Physiochim.* **1940**, *12*, 217–222.
90. Harkins, W.; Jura, G. Surfaces of solids XIII A vapor adsorption method for the determination of the area of a solid without the assumption of a molecular area, and the areas occupied by nitrogen and other molecules on the surface of a solid. *J. Am. Chem. Soc.* **1944**, *66*, 1366–1371. [CrossRef]
91. Halsey, G.D. The role of surface heterogeneity. *Adv. Catal.* **1952**, *4*, 259–269.
92. Tao, X.; Hu, X.; Wen, Z.; Ming, Y.; Li, J.; Liu, Y.; Chen, R. Highly efficient Cr(VI) removal from industrial electroplating wastewater over Bi2S3 nanostructures prepared by dual sulfur-precursors: Insights on the promotion effect of sulfate ions. *J. Hazard. Mater.* **2022**, *424*, 127423. [CrossRef]
93. Lagergren, S. Zur theorie der sogenannten adsorption geloster stoffe. Kungliga Svenska Vetenskapsakademiens. *Handlingar* **1898**, *24*, 1–39.
94. Ho, Y.S.; McKay, G.; Wase, D.A.J.; Foster, C.F. Study of the sorption of divalent metal ions on to peat. *Adsorpt. Sci. Technol.* **2000**, *18*, 639–650. [CrossRef]
95. Zeldowitsch, J. Über den mechanismus der katalytischen oxidation von CO and MnO_2. *Acta Physicochim.* **1934**, *1*, 364–449.
96. Weber, W.J.; Morris, J.C. Kinetics of adsorption on carbon from solution. *J. Sanit. Eng. Div. Am. Soc. Civ. Eng.* **1963**, *89*, 31–60. [CrossRef]
97. Boyd, G.E.; Adamson, A.M.; Myers, L.S. The exchange adsorption of ions from aqueous solutions by organic zeolites. *J. Am. Chem. Soc.* **1949**, *69*, 2836. [CrossRef] [PubMed]
98. Amirov, N.; Vakhshouri, A.R. Numerical modeling and optimization of product selectivity and catalyst activity in Fischer-Tropsch synthesis via response surface methodology: Cobalt carbide particle size and H2/CO ratio effects. *Int. J. Hydrogen Energy* **2020**, *45*, 31913–31925. [CrossRef]